

AUS Repository

Development and performance analysis of substrates coated with metal-organic framework for gas sensing applications

Item Type	Thesis
Authors	Al Abdulla, Shamma Saqer Ibrahim
Download date	2026-06-11 13:25:34
Link to Item	http://hdl.handle.net/11073/25326

DEVELOPMENT AND PERFORMANCE ANALYSIS OF SUBSTRATES
COATED WITH METAL-ORGANIC FRAMEWORK FOR
GAS SENSING APPLICATIONS

by

Shamma Saqer Ibrahim Al Abdulla

A Thesis presented to the Faculty of the
American University of Sharjah
College of Engineering
In Partial Fulfilment
of the Requirements
for the Degree of

Master of Science in
Mechanical Engineering

Sharjah, United Arab Emirates

April 2023

Declaration of Authorship

I declare that this thesis/ is my own work and, to the best of my knowledge and belief, it does not contain material published or written by a third party, except where permission has been obtained and/or appropriately cited through full and accurate referencing.

Signed.....Shamma Saqer Alabdulla.....

Date.....29/4/2023.....

The Author controls copyright for this report.

Material should not be reused without the consent of the author. Due acknowledgement should be made where appropriate.

© Year 2023

Shamma Saqer Ibrahim Al Abdulla

ALL RIGHTS RESERVED

Approvals

We, the undersigned, approve the Masters Thesis written by: Shamma Alabdulla

Thesis Title: Development and performance analysis of substrates coated with metal-organic framework for gas sensing applications.

Date of Defense: 26/4/2023

Name, Title and Affiliation	Signature
Dr. Mehdi Ghommem Associate Professor Department of Mechanical Engineering Thesis Advisor	
Dr. Rana Sabouni Associate Professor Department of Chemical and Biological Engineering Thesis Co-advisor	
Dr. Yassir Makkawi Associate Professor Department of Chemical and Biological Engineering Thesis Examiner (External)	
Dr. Wael Abuzaid Associate Professor Department of Mechanical Engineering Thesis Examiner (Internal)	

Accepted by:

Dr. Fadi Aloul
Dean
College of Engineering

Dr. Mohamed El-Tarhuni
Vice Provost for Research and Graduate Studies Office of
Research and Graduate Studies

Acknowledgements

I would like to thank my advisors Dr. Mehdi Ghommem and Dr. Rana Sabouni for their knowledge, advice, assistance, and motivation through my research journey. I would also like to thank Prof. Abdul Hai Alami from University of Sharjah for his continuous support and invaluable advice. I am grateful for their prolonged assistance and guidance, worthwhile discussion, and suggestions.

I would like to thank the professors of the Mechanical Engineering department for teaching me master's level courses with outstanding teaching techniques and skills. I value their incredibly useful advice and inspiration.

Lastly, I would like to thank the American University of Sharjah for giving me the opportunity to be a Graduate Teaching and Research Assistant. I would also like to acknowledge the assistance of the University of Sharjah's facilities including the Advanced Materials Research Laboratory.

Dedication


To my family and everyone who has supported me on this journey.

Abstract

This thesis investigates the potential use of Zeolitic Imidazolate Frameworks (ZIF-8) as a sensing material for CO₂ detection. Three synthesis techniques namely room temperature, microwave-assisted, and ball milling were explored for the preparation of ZIF-8. The latter is a green and facile alternative for synthesis with its solvent-free, room temperature operation. In addition, ZIF-8 samples produced through ball milling exhibited excellent CO₂ adsorption and detection characteristics, as confirmed by fluorescence measurements. To understand the structural morphology, the thermal stability, and elements content of the different ZIF-8 samples, a range of characterization tests including XRD, FTIR, TGA, FE-SEM and EDS were conducted. The characterization tests revealed the formation of a new phase of ZIF-8 (ZIF-L) when deploying the ball milling technique with different structure, morphology, response to CO₂ exposure and thermal stability compared to its counterparts. The ZIF-8 samples obtained from the different ZIF-8 samples were evaluated in terms of limit of detection (LOD), selectivity, and recyclability using fluorescence measurements. The ZIF-8 sample synthesized based on ball milling had a LOD of 815.2 ppm, while the LODs of samples obtained from microwave and room temperature-based synthesis techniques were 1780.6 ppm and 723.8 ppm, respectively. This shows that the room temperature and ball milling produced MOFs with comparable LODs. However, the room temperature procedure requires the use of methanol, a harmful solvent. The range of LOD demonstrates the suitable use of ZIF-8 for indoor air quality monitoring and other industrial applications. Finally, the ZIF-8 obtained from ball milling was coated on a substrate using ball milling at different milling speeds 100 rpm, 300 rpm and 500 rpm. The 300 rpm sample resulted in a favorable coating and CO₂ adsorption, thus, making it suitable to be deployed as a sensing layer for a miniature gas sensor.

Keywords: CO₂ detection; ZIF-8; MOFs; ball milling; fluorescence; coating; gas sensor.

Table of Contents

Abstract..... 	6
List of Figures	9
List of Tables	11
Chapter 1. Introduction.....	13
1.1. Introduction.....	13
1.2. Overview.....	13
1.3. Thesis Objectives	14
1.4. Research Contribution	15
1.5. Thesis Organization	15
Chapter 2. Background and Literature Review	16
2.1. Types of gas sensors.....	16
2.1.1. Carbon Materials - based gas sensors.....	16
2.1.2. Conductive polymer -based gas sensors.....	17
2.1.3. Acoustic wave sensors.....	18
2.1.4. Micro-thermal conductivity sensor.....	19
2.1.5. Catalytic sensors.....	19
2.1.6. Metal-oxide-semiconductor (MOS)-based gas sensors.....	20
2.1.7. Metal organic framework-based sensors.	21
2.2. Metal-Organic Frameworks for CO ₂ sensing	22
2.2.1. Synthesis methods.....	22
2.2.2. Physical properties	25
2.2.3. CO ₂ adsorption capacity	25
2.2.4. Kinetics of CO ₂ adsorption	27
2.2.5. CO ₂ selectivity	29
2.2.6. Characterization techniques (before and after deposition)	30
2.2.7. Limit of detection (LOD).....	32
2.2.8. Challenges related to the integration of MOFs in sensing devices.....	34
Chapter 3. Methodology	35

3.1.	Materials	35
3.2.	Synthesis of ZIF-8 using Microwave-assisted procedure (S1)	35
3.3.	Synthesis of ZIF-8 using room temperature procedure (S2)	35
3.4.	Synthesis of ZIF-8 using ball milling (S3)	36
3.5.	Characterization tests for the three synthesized MOFs.....	36
3.6.	Experimental procedure for CO ₂ detection, selectivity and regeneration....	36
3.7.	Substrate coating procedure	38
3.8.	Analysis of CO ₂ adsorption by the coated substrates	38
3.9.	Characterization of the coated substrates.....	40
Chapter 4.	Results and Analysis	41
4.1.	Characterization tests results.....	41
4.1.1.	XRD analysis	41
4.1.2.	FE-SEM/EDS analysis.....	42
4.1.3.	FTIR spectroscopy analysis	45
4.1.4.	BET analysis	46
4.1.5.	TGA analysis	47
4.2.	CO ₂ detection tests	49
4.3.	Coated substrate results.....	54
4.3.1.	FE-SEM/EDS results	54
4.3.2.	Gas chromatography results.....	56
Chapter 6.	Conclusion and Future Work.....	58
References.....		59
Appendix A.....		67
Vita.....		69

List of Figures

Figure 2-1: Image of the chemical sensor consisting of MWNTs. The CNTs are aligned in the electric field direction [16].	17
Figure 2-2: Microbalance sensor of quartz crystal during the interaction between the analyte and the sensing layer [23].	19
Figure 2-3: Illustration of n-type MOS gas sensor in air, oxidizing gas, and reducing gas [29].	21
Figure 2-4: Timeline of the different synthesis techniques for MOFs [32].	22
Figure 2-5: CO ₂ adsorption using hydrogen bonding with -NH ₂ functional group of the MOF [1].	26
Figure 2-6: π - π stacking interactions from MOFs and adsorbates [45].	27
Figure 2-7: Densities of different adsorbent materials with their pore sizes [49].	28
Figure 2-8: (a) MIL-96-(Al) framework, (b) MIL-96-(Al)-Ca framework, (c) and MIL-96-(Al)-Ca with CO ₂ or N ₂ adsorption [50].	29
Figure 2-9: (a) MIL53-AAO cantilever SEM image. (b) AAO cantilever surface before and (c) after fabrication of MIL-53. (d) XRD of the AAO substrate only (black), the MIL-53 (Al) deposited on the AAO cantilever (red), and XRD of the MIL-53 (Al) powder (blue) [2].	30
Figure 2-10: Co-MOF-74- TTF SEM image [52].	31
Figure 2-11: XRD patterns of Co-MOF-74 and Co-MOF-74-TTF compared with the simulated Co-MOF-74 [52].	32
Figure 2-12: IR microscopic images of CO ₂ adsorption using Co-MOF-74 and a Co-MOF-74-TTF crystal with increasing CO ₂ pressure: 50, 200, 500, and 1000 mbar (left to right) [52] simulated Co-MOF-74 [52].	32
Figure 3-1: The procedure used for fluorescence measurements.	37
Figure 3-2: (a) The experimental set-up and (b) the gas cylinders and flow controllers. controllers.	38
Figure 3-3: The procedure used for gas chromatography analyses.	39
Figure 3-4: The experimental set-up of CO ₂ exposure to the uncoated (control) and coated substrates.	40
Figure 4-1: XRD patterns for S1, S2, and S3 MOFs before and after CO ₂ exposure.	42

Figure 4-2: FE-SEM for ZIF-8 synthesized using S1, S2 and S3 before and after exposure to CO ₂ .	43
Figure 4-3: EDS color map of (a) S1 ZIF-8 before and (b) after, (c) S2 ZIF-8 before and (d) after, (e) S3 ZIF-8 before and (f) after CO ₂ exposure.	44
Figure 4-4: FT-IR spectra for ZIF-8 samples before and after CO ₂ exposure.	45
Figure 4-5: Adsorption isotherms of ZIF-8 synthesized using S1, S2 and S3, respectively, before and after exposure to CO ₂ .	46
Figure 4-6: TGA results of (a) S1, (b) S2, and (c) S3 ZIF-8.	48
Figure 4-7: Fluorescence intensity and Normalized Fluorescence of the S1, S2 and S3 ZIF-8 with different CO ₂ concentrations. Points represent the average of three trials and error bars represent the standard deviation of three trials.	50
Figure 4-8: Selectivity results of S3 MOF when exposed to CO ₂ and other gases.	53
Figure 4-9: Changes in the fluorescence intensity of the ZIF-8 (S3) upon exposure to CO ₂ over three cycles.	53
Figure 4-10: MOFs' turn-off in the water after being bubbled with CO ₂ at different concentrations and exposed to UV light.	54
Figure 4-11: SEM images of (a) carbon cloth sample, (b) the coated sample using 100 rpm, (c) 300 rpm, and (d) 500 rpm milling speeds.	55
Figure 4-12: EDS color map of (a) carbon cloth sample, (b) the coated sample using 100 rpm, (c) 300 rpm, and (d) 500 rpm milling speed.	56
Figure 4-13: Gas chromatography CO ₂ concentration in the test vials for coated ZIF-8 sample at different ball milling speeds and uncoated carbon cloth substrates.	57

List of Tables

Table 2-1: Comparison of different synthesis techniques [37],[38].	23
Table 2-2: MOFs synthesized by different procedures and their corresponding characteristics for CO ₂ sensing.	33
Table 4-1: Surface area and pore volume for the 3 samples before and after CO ₂ adsorption.	47

List of Abbreviations

EDS	Energy Dispersive X-Ray
FTIR	Fourier transform infrared
LOD	Limit of detection
MEMS	Micro-electromechanical systems
MOF	Metal Organic Framework
SEM	Scan Electron Microscope
XRD	X-Ray Diffraction

Chapter 1. Introduction

1.1. Introduction

In this chapter, an introduction about the gas sensing technology for monitoring harmful gas emissions is presented. The importance of having a highly sensitive and selective material for sensing applications is discussed. Then, the issues addressed by the current research are highlighted. Finally, the research contribution and the overall structure of the Thesis are discussed.

1.2. Overview

Gas sensors have shown significant growth in scientific communities. This is as result of their major role in monitoring harmful gas emissions with low concentrations such as carbon dioxide (CO₂) that has caused a great environmental concern in the recent years. Gas sensors convert the presence or concentration of the target gas into a resolvable signal via transduction techniques that can trigger the activation of safety functionalities [3]. These sensors are usually coated with a sensing material or a sorbent layer (e.g., polymer) with an affinity to the gas of interest to be detected. These sensing devices rely on the strong interaction of the gas analyte with the sensing material which enables the gas detection at low limits, and the working mechanism relies on the change in the material's properties while interacting with a target gas [4]. A sensing material should exhibit a high surface area and extremely reactive crystal site for particular gas molecules adsorption with maximum charge transfer[5]. Gas sensors are very useful for the following applications: Detecting environmental hazards [6], maintaining home and workplace safety [6], improving efficiency in food processing [6], protecting human well-being [6] and agriculture and aquaculture[7].

The performance of gas sensors can be assessed by several metrics such as sensitivity, resolution, and accuracy. Sensitivity refers to the change in the output per change in the input (measurand). Resolution is the smallest change in the input that can be detected. Accuracy determines the extent of uncertainty in measurement with respect to an absolute standard. The limit of detection (LOD) identifies the lowest amount of substance that could be measured by the sensor. Additionally, the response time indicates the specific time period required for the concentration to reach a specific limit that allows the sensor to produce a warning signal and the recovery time is the time it

takes for the sensing material to recover and returns its baseline status after the detection process [8].

The daily average concentration of CO₂ in the atmosphere reached 421 ppm worldwide in 2021 as reported in [9]. The combustion of coal, oil, and natural gas contribute to 80% of CO₂ emissions worldwide [10]. The rising concentration will not only affect human beings, but also the biological and industrial processes. In addition, the continuous exposure to indoors CO₂ at a level of 1000 ppm have been proven to cause inflammation and oxidative stress. Hence, monitoring the CO₂ gas leaks in indoor and outdoor environments with portable, efficient, and low-cost sensing devices is needed in several industrial sectors [11].

Gas sensors with high sensitivity and stability with lower limit of detection and response times, are crucial for such applications [12] [13]. Compatibility of the CO₂ sensors with room temperature is the other important factor in different applications including process control in food industry, air quality control, and biotechnology controls, etc. Particularly, the research and development on CO₂ detection using this mechanism is growing and can be sorted into two categories [4]:

- (i) Developing the sensing devices [4].
- (ii) Exploring and fabricating promising sensing materials [4].

The design of high performance materials for CO₂ detection should also be considered [14]. Therefore, exploring new materials with low energy penalty is vital [15].

1.3. Thesis Objectives

The objective of this work is to develop a sensing element with high sensitivity to CO₂ by preparing a substrate coated with metal-organic framework (MOF). The MOF, named ZIF-8, is synthesized using three different techniques and characterized. The sustainably synthesized MOF is then deposited on a substrate made of carbon cloth with varying the milling speed parameter and then its performance in terms of CO₂ adsorption is evaluated. Eventually, the element is designed to be integrated with a MEMS gas sensor that responds to small changes in mass. The scope of this research deals with the development of a sustainable procedure for synthesizing and coating the MOF to detect low concentrations of CO₂.

1.4. Research Contribution

The key contributions of this research work can be stated as follows:

- The development of a sustainable way to synthesize and deposit the MOF on a non-expensive and flexible substrate.
- Analyze the performance of the sensing system in terms of sensitivity and selectivity to CO₂, in addition to conducting fluorescence measurements to evaluate the limit of detection and recyclability of the MOF.

1.5. Thesis Organization

The thesis reminder is structured as follows: Chapter 3 provides background and literature review about the different types of gas sensors along with metal organic frameworks used for CO₂ sensing. In addition, the challenges related to the integration of MOFs in sensing devices are discussed. Chapter 4 describes the implemented methodology. The experimental setup is described in Chapter 5. The experimental results are reported and discussed in Chapter 6. Lastly, Chapter 7 concludes with a summary of the main findings of the present study and the future work.

Chapter 2. Background and Literature Review

In this chapter, we discuss the different types of gas sensors and metal-organic frameworks deployed for CO₂ sensing. Their synthesis, physical properties, and various CO₂ adsorption characteristics are presented. Finally, we highlight some challenges that arise in the integration of MOFs in sensing devices.

2.1. Types of Gas Sensors

Various materials were investigated for gas sensing depending on the requirements of the application of interest. Each type of gas sensor is expected to produce a response (output signal) when detecting the gas of interest. The types of gas sensors are explained in this section.

2.1.1. Carbon materials - based gas sensors

Carbon material in its various structures has been extensively investigated for gas sensing. The materials including carbon dot, carbon nanotubes (CNTs), graphene, and reduced graphene oxide (rGO), have demonstrated high surface area, high charge transfer at room temperature, stability and flexibility [5]. CNTs are mostly used as the conducting channel in chemiresistive sensors. The deposition of CNTs networks between two electrode occurs by different methods including solid transfer, printing, spraying, chemical vapor deposition (CVD) and drop-casting. The sensing response is detected by measuring the conductance between the electrodes. Surface atoms composition of CNTs allow the small change in the environment around the CNT to cause a detectable conductance change [16]. The nanotubes structure gives them intrinsically attractive electrical, physical, and chemical properties. They consist of single-walled carbon nanotubes (SWCNTs) and multiwalled carbon nanotubes (MWCNTs). SWCNT is composed of thick layer of graphite with one atom rolled into an ordered cylinder with several nanometers in diameter, and 1 to 100 microns in length. While MWCNTs are composed of several layers of graphite rounded together forming a tube shape, with the same central axis. MWCNT was investigated for CO₂ gas sensing by changing the concentration of CNTs and measuring the change in resistance. The device showed a significant increase in resistance due to the charge transfer between the CNT and CO₂ molecules. The high response time of 53.7 s was exhibited using 1.5 wt% of MWCNTs and a CO₂ concentration of 450 ppm in ambient

conditions [17]. Jang et al. used MWNTs for an NH₃ gas sensor. A silicon wafer substrate was used with a SiO₂ layer on top. The MWNTs were grown in CVD system and aligned between the Nb electrodes deposited on the substrate. Figure 2-1 illustrates the sensor's structures and the CNTs laterally placed along the electrodes [18].

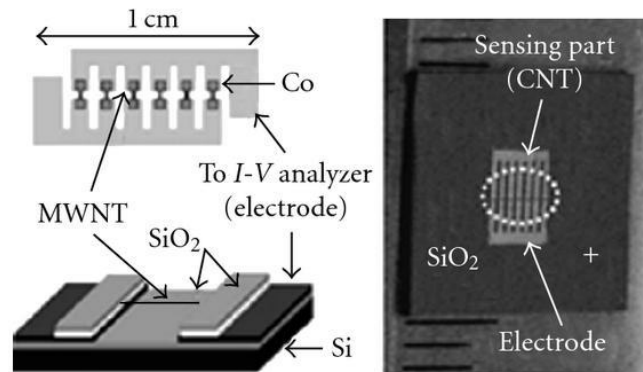


Figure 2-1: Image of the chemical sensor consisting of MWNTs. The CNTs are aligned in the electric field direction [18].

2.1.2. Conductive polymer -based gas sensors

Conducting polymers, including polypyrrole (PPy), polyaniline (Pani), polythiophene (PTh), have been utilized in gas sensors as the active layers due to their superior characteristics compared to sensors based on metal oxides and operating at high temperatures. The high sensitivities and short response time are exhibited at room temperature. The synthesis of these polymers can be performed through chemical or electrochemical methods. In addition, conducting polymers exploit good mechanical properties, which eliminates the complexity of sensors fabrication [19]. A CO₂ sensor composed of poly(3,4-ethylenedioxythiophene) (PEDOT) film and polyethylenimine (BPEI) layers was exposed to 1000 ppm CO₂. When the sensor was made of PEDOT layer only, the sensor exhibited no response. However, by integrating a BPEI layer the response increased to 3.25%. The sensor showed no decrease in response upon repeated usage, also, the response of the sensor showed higher selectivity for CO₂ than for O₂[20].

Based on previous studies, PPy and PANI show relatively higher sensing performance due to their nanostructure and small diameter providing high surface-to-volume ratio that enhances the diffusion rate of gas molecules and causing a high sensor response. The morphology of conducting polymer is an essential factor affecting the performance of the sensor. Doping was also observed to enhance the sensor response [21]. When exposed to a gas analyte, the electrical properties of the conductive polymer change while it adsorbs the molecules, and the sensing depends on the level of doping. Doping with an oxidizing agent causes the charge carriers to be added forming a p-type CP. Whereas an 'n-type doping' is induced by introducing a reducing agent. The conductivity of the CP material changes according to the electron transfer. For instance, an electron acceptor such as NO₂, extracts the electron from the polymer. For a p-type material, the conductivity and the doping level can be enhanced when interacting with these types of gases. Detecting an electron donating gas causes the reverse process to occur [22].

2.1.3. Acoustic wave sensors

The most known structure of the acoustic wave sensors is the delay line that consists of the transmitting and receiving transducer on a (piezoelectric) substrate. The sensitive part is placed between the transducers [23]. Surface acoustic wave (SAW) sensors have been used in recent times owing to their low costs, high precision, and adaptability with semiconductors [24]. In addition to their high resolution and stability, they constitute a facile frequency output signal approach [23]. The sensor is made of a sensing layer, the core of the sensor, and a conversion element (resonator or delay line). After the adsorption of the analyte, the response is obtained by measuring the frequency or phase shifts from the converter. Polymers, semiconductors, and graphene were highly used in SAW sensors as sensing films due to the sensitivity and selectivity they exhibit [24].

A new sensor based on quartz crystal, as shown in Figure 2-2, makes use of its physical-electrical properties. During absorption/adsorption of substances by the sensing layer on the surface, the frequency of the quartz crystal changes due to the mass increase on the surface [25].

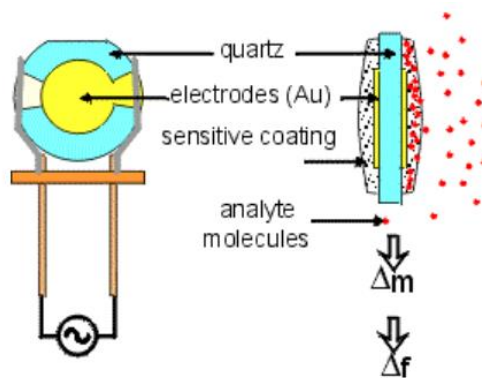


Figure 2-2: Microbalance sensor of quartz crystal during the interaction between the analyte and the sensing layer [25].

2.1.4. Micro-thermal conductivity sensor

The physical characteristics of a fluid are measured by a thermal conductivity detector (TCD) as it flows above an electrically heated resistive element. The resistive heating element is typically placed in a detection chamber. When various thermal conductivities of analytes occupy the chamber, the heat flux from the element changes, resulting in different electrical outputs [26]. Apart from calorimetric or metal oxide gas sensors, micro-thermal conductivity detector (TCD) gas sensors depend on variations in the thermo-physical characteristics of the surrounding gas instead of relying on gas adsorption and catalyst reactions. As a result, data can be obtained more quickly, and the sensor is able to be employed continuously and repetitively without memory effects. Miniature thermal conductivity gas sensors have been manufactured as detectors for gas chromatography (GC) devices, where the detector must respond immediately[27]. Cruz et al. [28] manufactured a μ TCD. A platinum heater was placed on a silicon nitride membrane in the model. At specific GC flow rates, the overall size of the membrane configuration was greater than 0.5 mm, and the sensors utilized nearly 1 W of power. To enhance the sensitivity, 4 TCDs in a Wheatstone bridge arrangement have been subjected to the reference stream, and column effluent and output voltage measurements were obtained while the input voltage was set to DC.

2.1.5. Catalytic sensors

A catalytic gas sensor is used to detect flammable gases or flammable vapors. The sensor operates by measuring the heat released from the gas combustion with oxygen on a miniature catalytic surface [29]. This causes an increase in the resistance

proportional to the concentration of the gas [30]. To address the of high-power consumption, catalytic sensors based on micro-technology have been developed to reduce the size and improve the response time while reducing the power consumption. Further advancements in the response time and sensitivity can be achieved by utilizing porous structures for the catalytic surface which results in increasing the reactive surface area and enhancing the reactivity of the catalyst layer, while reducing operating temperature and power consumption. Catalytic sensors with large surface areas exploit the use of nano-platinum thin film catalysts or, less frequently, palladium thin films and nanoparticles on aluminium oxide [31].

2.1.6. Metal-oxide-semiconductor (MOS)-based gas sensors

Gas detection using Metal-oxide-semiconductor (MOS) based sensors has been investigated over the last few years. However, further enhancements in the sensing characteristics need to be addressed to satisfy the requirements for particular applications based on medical diagnosis, gas detection, etc. , where high selectivity, low power consumption, fast response, low reliability on humidity and low limit of detection need to be achieved [32]. In addition, the reducing (H_2 , H_2S , etc.) or oxidizing (NH_3 , NO_2 , etc.) gas types and p-type or n-type semiconductors affect the performance of chemiresistive MO sensors. The energy released when an electron is added using an oxidizing gas for example, causes the adsorbed molecules on the MO layer to form anions [33]. The resistance of the semiconductor changes according to the following mechanism:

When an n-type semiconductor (see Figure 2-3) is exposed to oxygen ions (O^- , O^{2-}) these ions get adsorbed on the surface, resulting in the formation of a space-charge depletion region. The thickness of this region increases when the surface is exposed to an oxidizing gas, such as O_3 or NO_2 causing an increase in resistance, since oxidizing gases gain electrons from the MOS. On the other hand, a reducing gas, such as CH_4 and CO will give electrons to the MOS which reduces the resistance during the interaction with the adsorbed oxygen [33],[34].

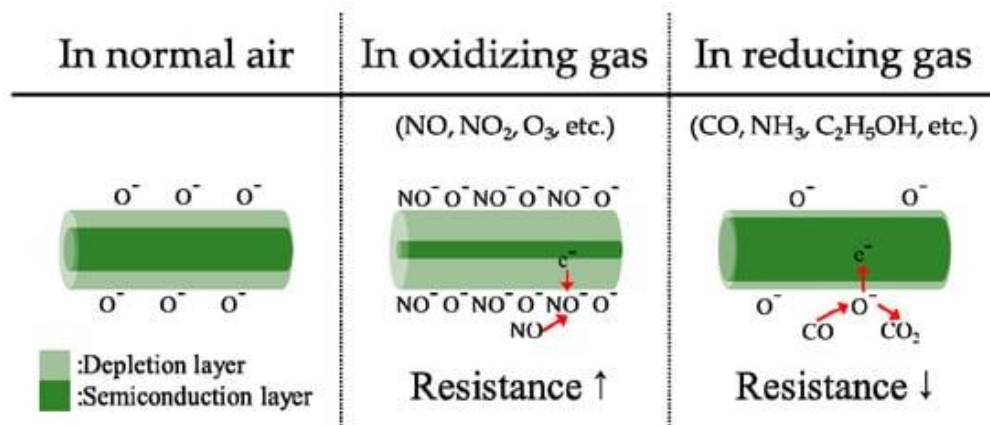


Figure 2-3: Illustration of n-type MOS gas sensor in air, oxidizing gas, and reducing gas [34].

2.1.7. Metal organic framework-based sensors

Metal organic frameworks (MOFs) consist of metal clusters connected by organic linkers. They exhibit large surface area which allows target gases to be adsorbed within their structure, which therefore enhances the selectivity of a gas sensor. Compared with traditional carbon-based and metal oxide-based sensors, MOF-based sensors exhibit several advantages such as operating at low to room temperatures, eliminating the need for high operating temperature, which consequently reduces the power consumption, making MOF-based sensors more-efficient and cost-effective to manufacture and be used in various sensing applications [11]. The gas detecting response can be quantified from the sensing layers through 1) mass or mechanical changes using microcantilevers and/or microresonator, 2) spectroscopic measurements, 3) changes in electric properties, 4) calorimetry, and 5) by color change [35]. Microresonator sensor utilizes the change in mass during an analyte adsorption to get the response through a change in resonant frequency. Villarroya et. al. [35] proposed a MEMS mass detection system that deploys several detection methods by using multiple cantilevers where the mass change is measured from the shift in resonance frequency. Infrared spectroscopy (IR) detects the analyte by transmission or reflection mode. In the transmission mode, the spectrum of the transmitted intensity of an infrared light by the sensing layer versus the frequency is used to quantify the variations that occur during the analyte adsorption. In the reflective mode, the sensing material is coated on a substrate that consists of a high relative refractive index optical material such as silicon. The reflecting times between the external surface of the silicon and the internal surface in contact with the material

allowing the beam to interact with the sample by transmitting an evanescent wave into the sample. This gives an indication on the amount of energy absorbed at each frequency [35]. The Refractive-index (RI)-based sensor is an optical sensor that has been mainly implemented for biochemical liquids sensing. However, for small gas sensing, its implementation is challenging due to the small RI change exhibited by variations of gas levels [7]. In contrast, electrical sensors exploit the changes in conductivity or resistance during the adsorption of an analyte within the material to monitor the changes in electrical properties of the sensing materials that consist of metal oxide guests [35]. Another type of chemical sensor is the luminescence-based chemical sensor, which detects particular chemical pollutants based on host-guest interactions, leading to sensing the desired molecules as low as the nanometer size range. Sensors composed of metal-organic frameworks (MOFs) materials are more appealing among these luminescence-based sensors because of their structural characteristics, functional content, and interactions between MOFs and analytes [36].

2.2. Metal-Organic Frameworks for CO₂ Sensing

2.2.1. Synthesis methods

Metal-organic frameworks (MOFs) possess 1-D, 2-D, or 3-D frameworks having high surface areas. The study of these materials has gained a lot of interest in different fields, due to their potential use in various applications. The synthesis procedures determine the structure and hence, the properties and resulting performance [37]. Figure 2-4 shows the timeline for the development of MOF's synthesis techniques.

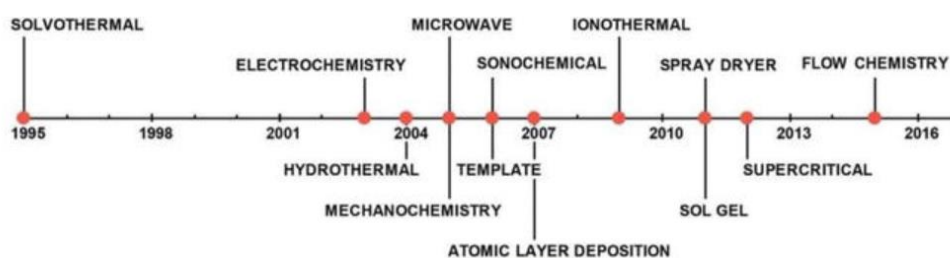


Figure 2-4: Timeline of the different synthesis techniques for MOFs [37].

Initially, MOFs were synthesized through solvothermal method where metal precursors and organic linkers are dissolved in solvent such N,N-dimethylformamide (DMF), N,N-diethylformamide (DEF), methanol, ethanol, and acetonitrile. Then these solutions are placed in a controlled reaction vessel, where the MOFs crystals form through

crystallization process. In general, the temperature during synthesis is maintained lower than 220°C, and the crystallization time differs from few hours to days [37].

Over the past few decades, great improvements have been made for MOFs synthesis. Various new methods have been developed, such as electrochemical, microwave-assisted, mechanochemical, microfluidic, etc. [37]. Some MOFs could just be synthesized at room temperature by mixing the starting materials, known as direct precipitation reaction, where the crystallization occurs within a short period of time [38].

Mechanochemical synthesis utilizes mechanical force for chemical synthesis. This process was recently proposed as an alternative for synthesizing MOFs while eliminating the use of toxic solvents, high temperature, and/or corrosive catalysts deployed in other synthesis methods [39]. The mechanochemical reactions provided from ball milling or grinding is considered as an efficient, fast with a high production rate (kilograms per hour) and clean way compared to the conventional solvent-based techniques for synthesis in wide areas including nanomaterials, pharmaceuticals and MOFs. Although there have been significant advancements in the synthesis methods, the mechanochemical reactions mechanism remains not fully understood. So far, applying continuous mechanical stress has been found to be the reason behind unusual reactivity different than that accessed from conventional chemistry [40],[41]. Table 2.1 shows a summary of the different synthesis techniques, their main advantages and disadvantages along with examples of MOFs.

Table 2-1: Comparison of different synthesis techniques [42],[43].

Synthesis Method	Conditions	Advantages	Disadvantages	Type of MOFs
Solvothermal	353-453K, 48-96 hours	-Technology can easily be commercialized. -Control on crystal growth. -Range of operating temperature is wide.	-High costs associated with synthesis. -Time needed for synthesis is long.	ZIF-95 ZIF-78

Microwave-assisted	303-373K, four mins- four hours	Crystallization time is reduced. -Reaction conditions are easy to control. -Particle size can be determined using precursor concentration.	-Not easily implemented in industry. -Single crystals are impossible to isolate.	IRMOF-1, IRMOF-2, IRMOF-3 Zr-UiO-66 Hf-UiO-66
Sonochemical	273-313K, 30 mins- 3 hours	-Can produce homogenous crystal size. -Can isolate the pure phase.	Large single crystals need to break for diffraction studies.	TMU-46, TMU-47, TMU-48
Mechanochemical	298K, 30 mins - 2 hours	-Synthesis can occur using a mechanical force only. -High temperature is avoided. -Free of harmful solvents.	-Single crystals are difficult to obtain for diffraction studies. -Secondary phases are usually produced.	Copper isonicotinate Cu(INA) ₂ Copper benzenetricarboxylate Cu ₃ (BTC) ₂ Cd(II)-based MOF
Electrochemical	273-303K, 10-30 mins	-Can easily be utilized in industry. -Less time for synthesis. -The morphology can be controlled using a current and voltage.	Synthesis is still in its early stage of development.	UiO-66 Cu ₃ (BTC) ₂
Slow diffusion	298 K, 7 days – 7 months	-Large single crystals are prepared. -Ambient or low operating temperature is needed.	Synthesis happens for a long time.	Zn ₃ (BDC) ₃ ·6CH ₃ OH

2.2.2. Physical properties

The properties of MOFs can be tuned by selecting proper starting materials. This causes the materials to either absorb small molecules or to add larger species. In addition to the selection of the structure elements, the way they are connected together is also important. The properties of the synthesized MOFs can be predicted from a framework formation by the building units [44].

The synthesis process was examined in several research studies with the goal to modify the chemistry, stability, particle size, and mobility of the framework. To further improve the properties, a “Post- synthetic modification” can be applied to the MOFs. MOFs are well-known for their high porosity and surface area. The desired pore size and configuration of the framework can be obtained by choosing a suitable linker and metal cluster [44]. Compared with carbon-based and metal oxide-based sensors, MOF-based sensors do not require high operating temperatures and showed high performance in low/room temperatures, which consequently reduces the power consumption, makes it easy to manufacture and allows it to be used in various application areas [11].

2.2.3. CO₂ adsorption capacity

The efficient MOF materials for CO₂ adsorption from atmosphere should exhibit high CO₂ adsorption capacity and selectivity at ambient pressure. In addition, these MOFs should be resistant to water and acid gases and must be regenerated for repeated use. High volumetric adsorption capacity for CO₂ is also crucial when it comes to practical utilization [45]. In porous materials, the CO₂ adsorption is improved by using Amines due to the acid-base interaction, electrostatic forces, or dispersion forces. MOFs containing basic nitrogen organic groups were investigated for their CO₂ adsorption characteristics [10].

The increase in the total basicity of the materials is associated with higher CO₂ uptake capacity, this is related to the Lewis acid behavior of the gas. Amine functional groups have been shown to have a strong interaction with acidic CO₂ group and incorporating these groups into MOFs can improve their CO₂ adsorption capacity. For instance, a Cu-based MOF functionalized with and 2-aminoterephthalic as a linker showed a better CO₂ adsorption capacity of 5.85 mmol g⁻¹ at 25 °C compared to Cu-BDC MOF. This is due to the existence of NH₂ group that enhances the CO₂ adsorption [46]. The electrostatic interactions are often used for substance adsorption process from

wastewater. The electric charge of MOFs (cationic or anionic) allows them to interact with oppositely charged adsorbates. [1]. For example, CO₂ reduction driven by electrostatic attraction was investigated using an anionic Cu-HHTP host, where HHTP = 2,3,6,7,10,11-hexahydroxytriphenylene, and a cationic photosensitizer [Ru(phen)₃]²⁺ (phen = 1,10-phenanthroline) used as a guest which resulted in a high photocatalytic activity for CO₂ reduction under a light source or natural light, due to the electrostatic interactions that enhance the charge transfer [47].

Hydrogen bonding is a mechanism known for CO₂ adsorption. It occurs when the oxygen electron pair from the CO₂ molecule bond with hydrogen atoms in the functional group of -NH₂ (see Figure 2-5).

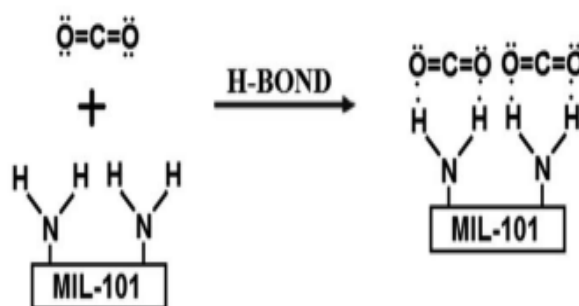


Figure 2-5: CO₂ adsorption using hydrogen bonding with -NH₂ functional group of the MOF [1].

Hydrophobic interactions occur when non-polar molecules with low solubility and long carbon chains are used for adsorption in an aqueous medium [1]. ZIF-8 is an example of a MOF with good water stability, the hydrophobic group consists of methyl group on the ligand and helps in preventing water molecules from attacking the [ZnN₄] units. In addition, water resistance is high in ZIF-68, 69, and 70 MOFs [48]. The hydrophobic nature subsequently assists in preventing decomposition and lowered capacities [10].

Besides hydrogen bonds, the intermolecular interactions of π - π stacking, shown in Figure 2-6, are also important, although they are weaker [49]. The heteroaromatic systems such as pyrrole, thiophene, imidazole and indole exhibit extreme π - π stacking interactions with carbon dioxide. Indole shows the largest CO₂ bond energy (16.7 kJ/mol). These systems are used as functional materials for CO₂ adsorption. The

aromatic systems stacking forms with CO₂ consists of the electronegative aromatic ring and CO₂ electropositive central C atom interaction and the H-bond interaction occurring with an electropositive aromatic H atom and an electronegative O atom from the CO₂, in addition to the dispersion interaction [50]. CO₂ and MOFs/ZIFs interactions are highly increased by π - π interaction between the CO₂ and aromatic rings [51].

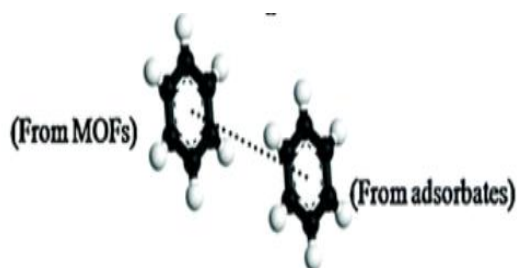


Figure 2-6: π - π stacking interactions from MOFs and adsorbates [49].

2.2.4. Kinetics of CO₂ adsorption

The diffusion rates affect the kinetic separation and depends on different factors such as, the size and shape of molecules as well as the pore, the interactions of specific adsorbents sites to the adsorbate's molecules, the input's chemical components, operating temperature, etc. The difference of diffusivity determines the ability of adsorbents to separate two or more components. In adsorption based on kinetic mechanism, the components adsorbed slowly should not resist the rapid diffusion of adsorbed molecules. A study reported the adsorption of CF₄/Ar mixtures through CuBTC and RPM1-Co. When diffusing through Cu-BTC channel, neither component faced any resistance and hence, diffused through the MOF. On the other hand, the argon molecules were diffused faster in RPM1-Co than CF₄, leading to a faster adsorption. Therefore, RPM1-Co is said to be capable of kinetic-driven separation between Ar and CF₄ molecules [52].

Another important point is that the larger mass molecules diffuse rate is lower in pores that have a diameter less than that of the mean free path. This is the case for gas molecules in microporous materials. For instance, when a mixture of CO₂/CH₄ was

investigated for kinetic adsorption on a Zn-based MOF, the CH₄ molecules adsorption rate was faster than CO₂ molecules [52].

Materials like Zeolites, activated carbon, and MOFs provide high CO₂ adsorption kinetics rates. This may be attributed to the narrow pore sizes. For example, a pore size smaller than 4 Å exhibit high potential to separate CO₂, gas with high diffusion rate, from other slowly diffusing molecules, such as CH₄ and N₂. The narrow size of the pore (close to CO₂ molecular size) will allow slow diffusion of the larger probe molecules, including CH₄, N₂ and O₂. However, the synthesis of these materials is challenging [53].

At medium and high pressures, microporous adsorbents with high surface areas and large pore volumes of 0.8-2 nm pore sizes exhibit high CO₂ adsorption and fast kinetics, however their selectivity for CO₂ is low. On the contrary, adsorbents with small pore sizes (0.35-0.8 nm), low surface areas, and small pore volumes have low CO₂ uptake at high pressure but considerably higher selectivity at low pressures (0.05-0.15 bar) [53]. Therefore, pore size reduction have been seen to enhance the CO₂ separation performance by allowing optimal gas diffusion through the large pore opening. Further reducing the pore size to 0.33 nm have been found to improve CO₂ selectivity by gas diffusion [53]. Furthermore, the density of the material increases with reducing the pore size. Figure 3-7 shows the densities of different adsorbent materials with their pore sizes. When narrow pore sizes and high charge density SiF₆ materials were used for CO₂ adsorption at low pressures, they showed high volumetric uptake (10% CO₂) [53].

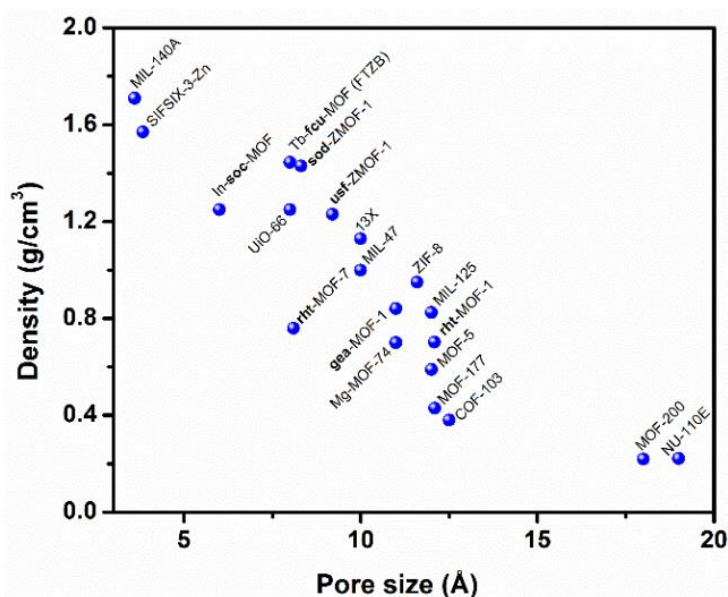


Figure 2-7: Densities of different adsorbent materials with their pore sizes [53].

2.2.5. CO₂ selectivity

The selectivity based on adsorption occurs due to the difference in the affinity of the gas molecules to be adsorbed by the MOF on the pore. Physisorptive adsorption's selectivity relies on the difference in physical properties of the molecules, including polarizability or the quadrupole moment, this causes the enthalpy of adsorption to be higher in certain molecules over others. In post-combustion CO₂/N₂ separation, CO₂ had higher polarizability and quadrupole moment (CO₂, $29.1 \times 10^{-25} \text{ cm}^{-3}$; N₂, $17.4 \times 10^{-25} \text{ cm}^{-3}$) and (CO₂, $13.4 \times 10^{-40} \text{ C} \cdot \text{m}^2$; N₂, $4.7 \times 10^{-40} \text{ C} \cdot \text{m}^2$) compared with N₂, which consequently results in higher selectivity for CO₂ [10]. Selectivity can be also dictated by the chemistry involved with certain molecules of the gas and the MOF surface activities. Higher selectivity can be obtained from the tendency of these molecules to participate in specific chemistry compared with physisorptive techniques. For instance, the interaction of CO₂ with a strong Lewis bases such as amines in CO₂/N₂ gas mixture results in bonding between C-N as detected from the aqueous amine solutions, which indicates a high selectivity of CO₂ over N₂ [10]. The coordination of a second metal such as in Aluminum trimesate-based MOF (MIL-96-(Al)) where Ca was added is found to enhance the CO₂ selectivity. By increasing the Ca²⁺ content in MIL-96(Al)-Ca₄, the pore volume was increasing and the CO₂ adsorption decreased, however, the selectivity of the adsorbent for CO₂ was much higher over N₂ due to the Lewis base-calcium oxide incorporation on the metal center, as seen in Figure 2-8. Therefore, providing high selectivity when compared with other reported adsorbents [54].

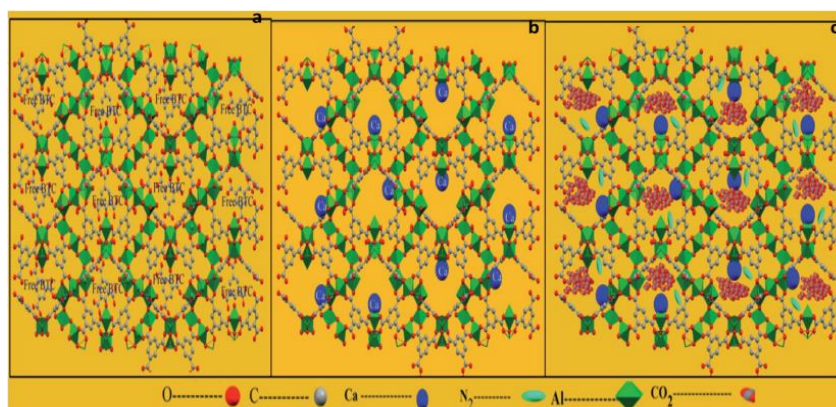


Figure 2-8: (a) MIL-96-(Al) framework, (b) MIL-96-(Al)-Ca framework, (c) and MIL-96-(Al)-Ca with CO₂ or N₂ adsorption [54].

2.2.6. Characterization techniques (before and after deposition)

Various sensing layers utilizing MOFs were used for CO₂ detection. The surfaces of the substrates were characterized before and after to show the deposition of the MOFs. For example, aluminium was anodized producing microcantilevers of nanoporous anodic aluminium oxide (AAO), then MIL-53 (Al) MOF layers were synthesized on each cantilever surface and was exposed to N₂, CO, Ar and CO₂, resulting in deflections as a response to the CO₂ adsorption. The scanning electron microscopy (SEM) characterization of MIL53-AAO Microcantilevers was applied at different magnifications. The aluminium oxide layer on the cantilever was converted to MIL-53 (Al) by hydrothermal reaction. From the SEM image in Figure 2-9 (a), (b), and (c), the MIL-53 layer consists of granules with diameter of hundred nanometers. The X-ray diffraction (XRD) image show that there are no peaks for the AAO substrate, while there are two peaks, (022) and (211), that of the MIL-53 layer on the AAO substrate, as seen in figure 2-9 (d), this proves that the MOF has a crystalline structure. The thickness of the AAO substrate, which is 2 μm, is insignificantly affected by the growth of the MIL-53 layer (100 nm thick) [2].

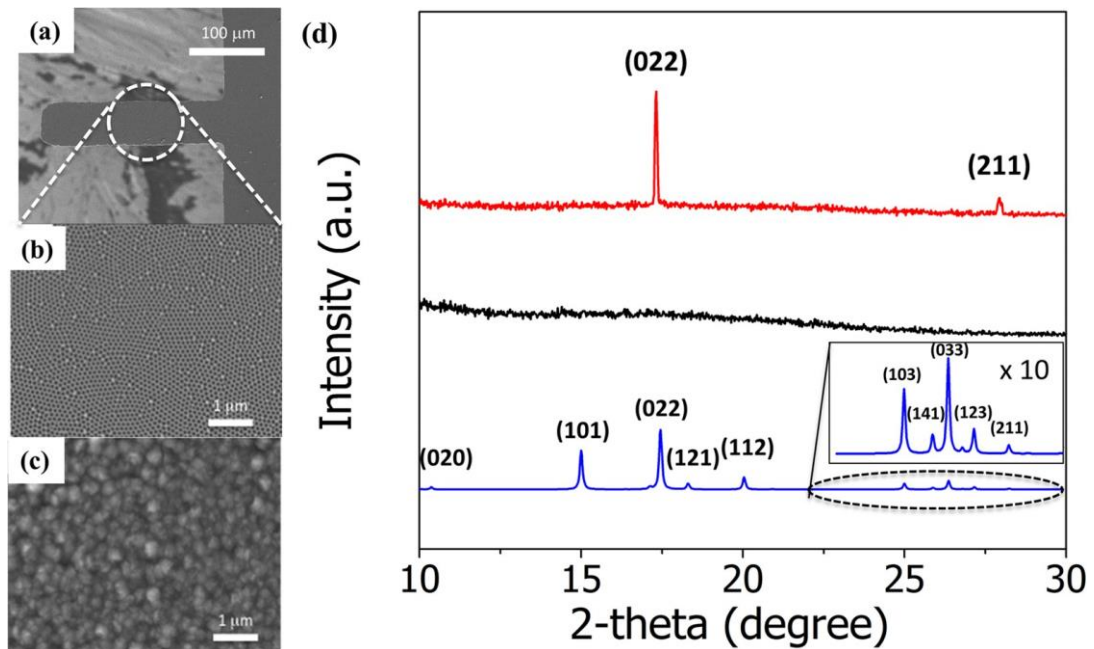


Figure 2-9: (a) MIL53-AAO cantilever SEM image. (b) AAO cantilever surface before and (c) after fabrication of MIL-53. (d) XRD of the AAO substrate only (black), the MIL-53 (Al) deposited on the AAO cantilever (red), and XRD of the MIL-53 (Al) powder (blue) [2].

The incorporation of tetrathiafulvalene (TTF) organic semiconductor into Co-MOF-74 powder was investigated in resistive gas sensing. X-ray diffraction and scanning electron microscopy were used to characterize the crystal structure of Co-MOF-74-TTF. The SEM in Figure 2-10 shows the Co-MOF-74-TTF rodlike crystal with a 20 μm width and 70 μm length. Co-MOF-74 pores have a diameter of 1.1–1.2 nm that are placed along the long axis. XRD was done to depict the crystal structure of Co-MOF-74-TTF. Figure 2-11 shows the difference in the XRD of Co-MOF-74 and Co-MOF-74-TTF to the simulated Co-MOF-74. The crystal structure of the infiltrated MOF is similar to the non-infiltrated but has a small shift to a lower 2θ value. The IR microscopic images shown in Figure 2-12 display the CO_2 adsorption on the Co-MOF-74 alone and the Co-MOF-74-TTF composite crystal at a CO_2 pressure of 50, 200, 500, and 1000 mbar (left to right). For Co-MOF-74, it is clearly shown that there is a notable increase of the CO_2 adsorption which appears when increasing the gas pressure up to 1000 mbar (left to right). On the other hand, the Co-MOF-74-TTF did not display a high difference in CO_2 adsorption with higher CO_2 pressures since a portion of the pore volume was blocked by the TTF. However, the electrical conductivity increased with the Co-MOF-74-TTF during interaction with the gas molecules [55].

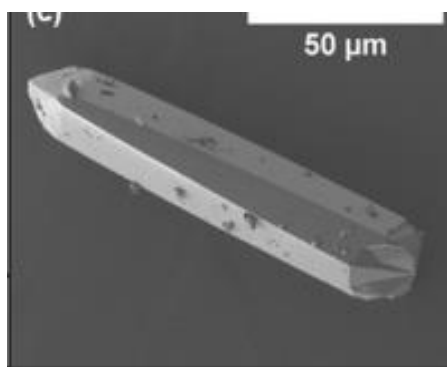


Figure 2-10: Co-MOF-74-TTF SEM image [55].

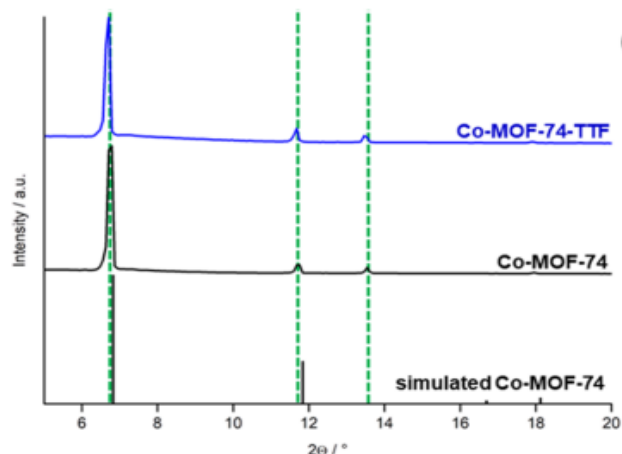


Figure 2-11: XRD patterns of Co-MOF-74 and Co-MOF-74-TTF compared with the simulated Co-MOF-74 [55].

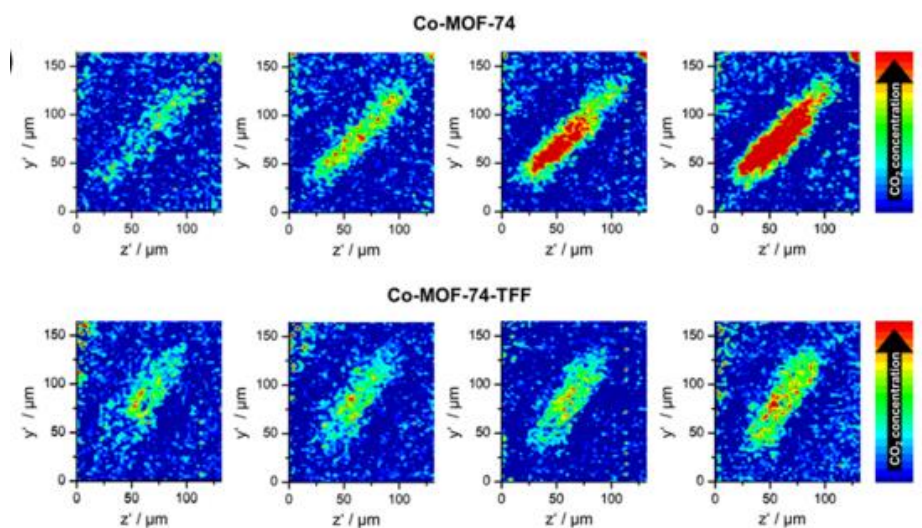


Figure 2-12: IR microscopic images of CO₂ adsorption using Co-MOF-74 and a Co-MOF-74-TTF crystal with increasing CO₂ pressure: 50, 200, 500, and 1000 mbar (left to right) [55].

2.2.7. Limit of detection (LOD)

Few studies have reported the employment of MOFs for CO₂ sensing and identified their limit of detection [56]. For instance, Wang *et al.* reported a limit of detection of 20 ppm for CO₂ when using near-infrared (NIR) optical fiber coated with HKUST-1 [57]. Additionally, Huang *et al.* developed an enhanced Raman scattering (SERS) based sensor with ZIF-8 MOF films that resulted in a LOD of 5×10^{-8} M with an eight minute response time. The SERS-based sensor was capable of detecting different

analytes at low concentration. Moreover, a sensor consisting of MOF films grown on-chip on Pt interdigitated electrodes using solvothermal approach was used for benzene and CO₂ detection at room temperature. The LOD for CO₂ of the modified Mg-MOF-74, also known as [Mg₂(dobdc)(H₂O)₂] where dobdc = 2,5-dihydroxy-1,4-benzenedicarboxylate, was 200 ppm [35]. The newly developed UiO-66-ONa fluorescent MOF has shown a significant performance for CO₂ sensing due to interaction of sodium phenolic group with CO₂, resulting in a LOD of 3.5×10^{-7} M [12]. Table 2.2 provides a summary of different MOFs and their corresponding characteristics for CO₂ sensing.

Table 2-2: MOFs synthesized by different procedures and their corresponding characteristics for CO₂ sensing.

MOFs	Synthesis	CO ₂ capacity	CO ₂ selectivity	Limit of Detection	Reference
ZIF-8	-	-	High	5×10^{-8} M	[9]
Co(II)-MOF	Solvothermal	-	High	-	[58]
ZrFSIX-2-Zn-i	Solvothermal	4.56 mmol g ⁻¹	High	-	[59]
Al-MIL-53 + conductive carbon	Solvothermal	-	High (over CH ₄)	-	[60]
MIL-101(Cr, Mg)	Solvothermal	Reached 3.28 mmol /g at 298 K and 1 bar	High over N ₂ , enhanced up to 86 at 100 kPa	-	[61]
dmen- Mg ₂ (dobpdc) (dmen = <i>N,N</i> - dimethylethylen ediamine)	Microwave	At 25 °C and 0.15 bar, 1- dmen take s up 3.77 mmol g ⁻¹ of CO ₂	High over N ₂ .	-	[62]
Cd(II)	Solvothermal	CO ₂ uptake is 27.5 cm ³ g ⁻¹ at 273 K and 1 bar	High over CH ₄ .	-	[63]

Cu-BTC	Solvothermal	-	-	500ppm	[64]
MIL-101(Cr)	Hydrothermal	3.16 mmol /g	-	-	[65]
Zeolitic imidazolate framework-8 (ZIF-8) nanoparticles	Solvothermal	Greater at lower temperature	Greater over N ₂ at lower temperatures	3130 ppm at room temperature and 774 ppm at 278 K.	[66]

2.3. Challenges Related to the Integration of MOFs in Sensing Devices

One of the main issues is the integration of MOFs into devices due to their poor performance exhibited from detection of water in open atmosphere and their low water stability under humid conditions. To address this issue, researchers suggest prioritizing stability over high sensitivity by utilizing more water stable MOFs [9]. Moreover, environments with high operating temperature increases the complexity of the gas sensing system due to problems associated to stability, selectivity and difficulty to use in flammable spaces. Although gas sensors based on MOFs exploit many sensing properties, they are not yet commercially available. Future research should focus on integrating MOFs with flexible substrates, and stability of the device for the long-term usage [67].

Chapter 3. Experimental Methodology

In this chapter, the synthesis procedures and experimental setup used to develop sensitive MOFs to CO₂ using three different techniques, namely microwave-assisted, room temperature and mechanical ball milling, are discussed. The process of coating and testing the sensing element is also presented.

3.1. Materials

The gases used for the experiments are Argon (99.998%), CO₂ (99%), and Nitrogen (99.998%) which were obtained from Caltrols Middle East LLC. All Chemicals were obtained from LabCo, the local supplier for Sigma Aldrich in the UAE and used without any further modification. The materials include zinc nitrate hexahydrate (Zn(NO₃)₂·6H₂O, 99%), 2-methylimidazole (CH₃C₃H₂N₂H, 99%), and dimethylformamide (DMF). The preparation of the MOF takes three main routes: (i) microwave-assisted (S1), (ii) room temperature (S2) and (iii) mechanical ball milling (S3) approaches. These will be detailed in the following sections.

3.2. Synthesis of ZIF-8 Using Microwave-Assisted Procedure (S1)

The previously described method by Hillman [68] was used for the microwave synthesis with the modest modification of doubling the amount of materials. In 15 ml of methanol, 0.65g of zinc nitrate hexahydrate was dissolved. Then, 15 ml of methanol was also used to dissolve 0.73g of 2-methylimidazole. The resultant solution was then put into a 50 ml Teflon-lined microwave reaction vessel that was designated for microwave irradiation and microwaved using the laboratory Microwave of the model MDS-6G Digestion, obtained from a Chinese manufacturer of Laboratory equipment, Sineo, for 90 seconds at 100 W. After that, it was centrifuged, washed three times with methanol, and overnight dried in an oven at 80 °C.

3.3. Synthesis of ZIF-8 Using Room Temperature Procedure (S2)

The synthesis was carried out in accordance with the previously published method by Hunter-Sellars et. al. [69], in which 1.642g of 2-methylimidazole was dissolved in 50 ml of methanol and combined with 0.745g of zinc nitrate hexahydrate dissolved in 50 ml of methanol. After being centrifuged and thoroughly washed with methanol three

times, the precipitate was dried under vacuum for the next 24 hours at room temperature.

3.4. Synthesis of ZIF-8 Using Ball Milling (S3)

The Pulverisette 7 planetary ball mill from Fritsch's premium line was used to synthesize the MOF using ball milling. The amount of ligand and metal cluster were obtained from Hou et al. earlier work [9], although the synthesis method was modified without the addition of solvents. Two 7mm diameter stainless steel balls were added in the ball mill with 1.484g of $Zn(NO_3)_2 \cdot 6H_2O$ and 3.278g of Hmim for an hour. The ball mill was run at its maximum speed of 1100 rpm. After that, the sample was centrifuged. The created milky dough was washed with methanol and dimethylformamide (DMF) to get rid of any remaining metal ions and ligands. Subsequently, the sample was dried for four hours at 100°C in the oven.

3.5. Characterization Tests for the Three Synthesized MOFs

5 mg of all the resultant MOFs were used for characterization before and after exposing to CO_2 for five minutes. The Bruker D8 Advance DaVinci multifunctional X-ray diffractometer with Cu K radiation operating at $\lambda = 1.5406 \text{ \AA}$, 40 kV tube voltage, and 40 mA current was used for the X-Ray Diffraction (XRD) test. The 5.0° to 40.0° range with a step size of five, is where the XRD patterns are captured at $\Delta\theta = 25^\circ$. TESCAN's VEGA3 XM is used for EDS analysis which runs at 5 kV operating voltage for both map and point modes. The FE-SEM analysis was done using JEOL JSM-7500F FESEM at 3 kV. TGA-50 Series from SHIMADZU was used for thermogravimetric analysis under temperature range from 25°C to 800°C with heating rate of 5°C/min. FTIR analysis was conducted using JASCO FT/IR-6300 Fourier transform infrared spectrometer in the range (4000-400 cm^{-1}) to identify the chemical composition and physical state of the samples. Surface area and adsorption-desorption isotherms were performed using Autosorb iQ utilizing multipoint Brunauer Emmet Teller (BET) method. The pore volume was reported using density functional theory (DFT) method. Samples were degassed under vacuum at 150° C for 15.4 hr.

3.6. Experimental Procedure for CO_2 Detection, Selectivity and Regeneration

The DW-F97Pro Fluorescence Spectrophotometer obtained from Drawell was used to test the fluorescence intensity of the prepared ZIF-8 suspension before and after

exposure to CO₂. A suspension of the fluorescent probe (ZIF-8) of 100mg/l was prepared by sonicating 5mg of the ZIF-8 in 50ml of deionized for 15 min to ensure full suspension of the MOF particles. Then, 3ml of the mixture was taken for fluorescence measurement at 300-600nm using excitation wavelength of 240nm. The baseline before CO₂ exposure was recorded for each synthesized MOF. The detection measurements were performed through bubbling CO₂ into 3ml of the MOF suspensions at different concentrations for 20s. The experimental procedure is illustrated in Figure 3-1. The fluorescence efficiency was obtained using Equation (1):

$$\frac{I}{I_0}\% = \frac{I_{immediate}}{I_{baseline}} \times 100 \quad (1)$$

Where $I_{baseline}$ is the initial intensity of the MOF with water before exposing it to the analyte, and $I_{immediate}$ is the fluorescence intensity after exposing the MOF to the gas analyte [70].

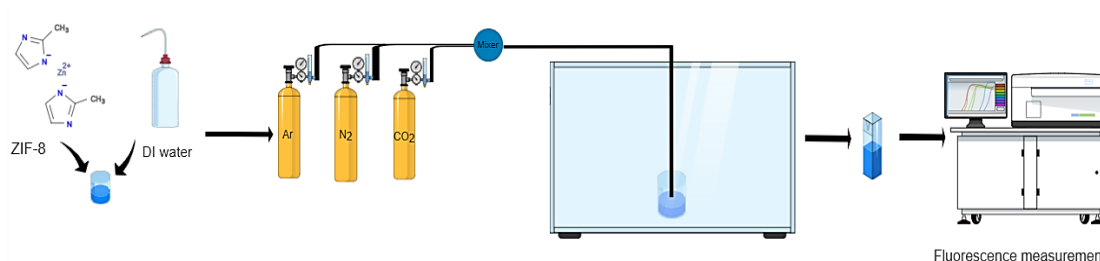


Figure 3-1: The procedure used for fluorescence measurements.

A series of tests were run to assess the performance of the three MOFs in various controlled environments. Figure 3-2 illustrate the experimental setup. The MOFs were first examined with CO₂ bubbled by a gas cylinder in a beaker which was carefully closed before taking the readings. Using high-resolution mass-flow controller obtained from Caltrols Middle East LLC, the amount of the gas was increased. In each case, the three trials were averaged and the standard error was taken. For the selectivity experiments, other gases including N₂, Ar and air (as shown in the Figure) were compared to CO₂ by measuring the fluorescence intensity at a fixed flow rate of 0.15 l/min. Finally, the regeneration experiments were conducted to investigate the recyclability of the MOF and its capability to maintain a good detection level of CO₂

by observing the quenching and recovery of the fluorescence intensity upon the injection of CO₂ and N₂, respectively. The regeneration experiments were performed for three cycles. All experiments were conducted at room temperature.

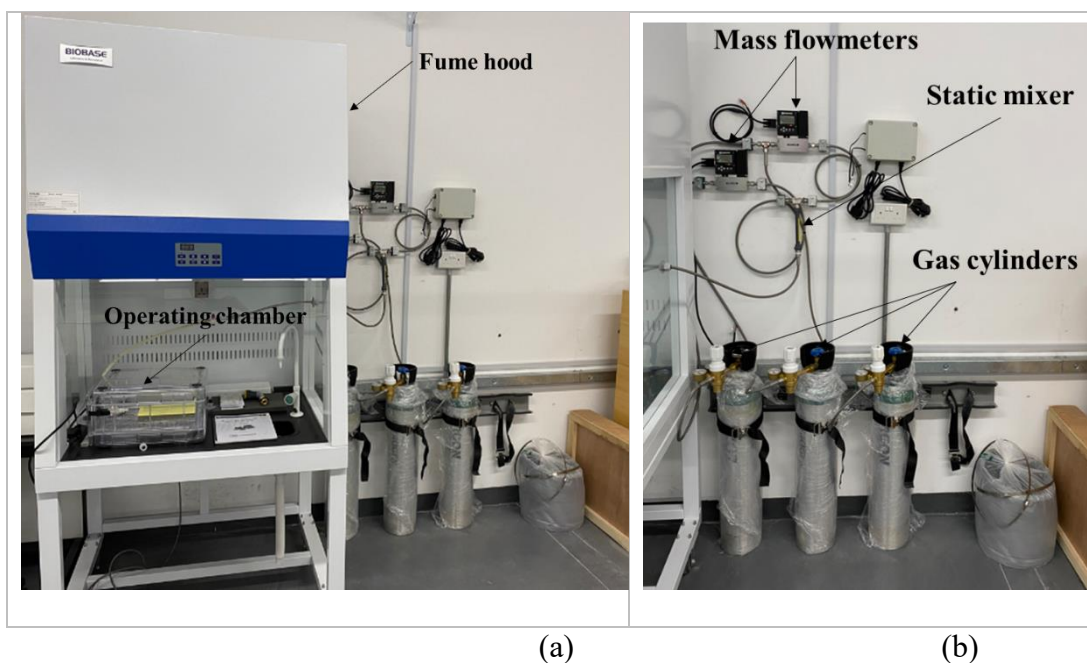


Figure 3-2: (a) The experimental set-up and (b) the gas cylinders and flow controllers.

3.7. Substrate Coating Procedure

Three carbon cloth substrates were used with a dimension of 3 cm × 1.5 cm to deposit 800 g of the MOF produced from ball milling on each sample also using ball milling. In this process, the kinetic energy of the small MOFs particles was utilized to coat the sensing layer. In order to test the impact of the coating structure on the behaviour of the sensing element, the milling speed was varied while fixing the mass of the powder. The three milling speeds used were 100, 300 and 500 rpm, for a duration of five minutes.

3.8. Analysis of CO₂ Adsorption by the Coated Substrates

The CO₂ gas cylinder as shown in Figure 3-3, was exposed to the samples in the test vials before taking them for gas chromatography analysis to inspect the concentration of gas left in the bottle. The three coated samples are also shown in the Figure, where

Coating 1, Coating 2, and Coating 3 represent the samples coated using 100 rpm, 300 rpm and 500 rpm milling speed.

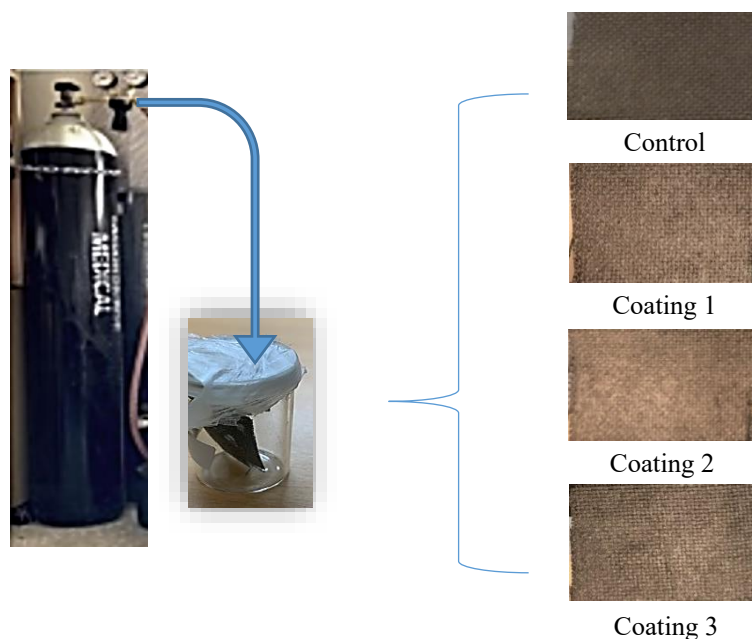


Figure 3-3: The experimental set-up of CO₂ exposure to the uncoated (control) and coated substrates.

To examine the CO₂ adsorption by the three different substrates, the gas was exposed to a control sample (uncoated carbon cloth) and to each coated sample under controlled parameters of 10s (total injection time) and a flow rate of 1 l/min. To measure the amount of CO₂ adsorbed by the coated and uncoated substrates, gas chromatography analysis was applied. Samples of gas mixture inside the bottle after the adsorption of CO₂ by the substrate were collected using a syringe.

3000 Micro GC in addition to INFICON EZ IQ chromatography software from INFICON are used for the chromatography analysis to identify the target compounds by calculating the maximum observed area in a chromatogram which is then used to calculate the concentration. The peak area is proportional to the amount of analyte identified. For GC separation, two capillary columns are employed: Porous Layer Open Tubular (PLOT) and Wall Coated Open Tubular (WCOT). A calibration curve utilizing calibration gases can be used to determine the concentration of the target [71]. The detection ranges from low concentrations to higher percentages. The concentration of the gases is measured in mole %. The procedure used to conduct this analysis is illustrated in Figure 3-4.

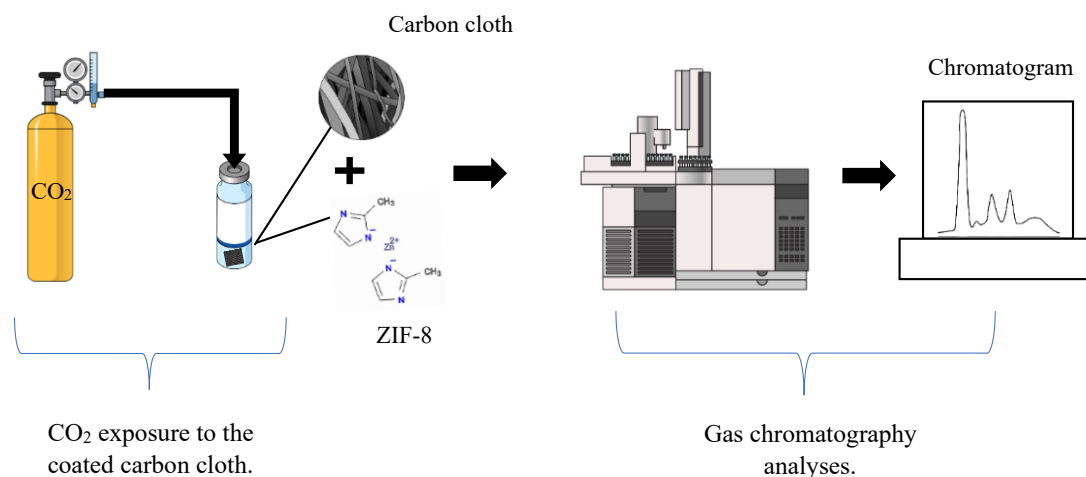


Figure 3-4: The procedure used for gas chromatography analyses.

3.9. Characterization of the Coated Substrates

The same TESCAN's VEGA3 XM is used for EDS analysis at 5 kV operating voltage for both map and point modes, and JEOL JSM-7500F SEM at 3 kV. The advantages of implementing this analysis is to inspect the properties of the coated surfaces to allow the structure visualization of the coating and the elements distribution within the scanned area.

Chapter 4. Results and Analysis

In this chapter, we present and analyse the main features of the developed MOF as obtained from the characterization tests along the CO₂ detection, selectivity and regeneration results. We also discuss the performance of the coated substrate in terms of CO₂ adsorption.

4.1. Characterization Tests Results

4.1.1. XRD analysis

The XRD patterns of the ZIF-8 samples prepared using the three different synthesis techniques, before and after exposure to CO₂ are shown in Figure 4-1. The crystal structure of the three synthesized MOFs are in close agreement with previous studies and confirm the phase purity [72]. The XRD patterns of the MOFs obtained from S1 and S2 indicate the sodalite structure of the material [72],[73] with sharp peaks at 2θ of 7.30°, 10.35°, 12.70°, 14.80°, 16.40° and 18.00° [74]. An alteration in the structure after adsorption of CO₂ is observed. For the MOF produced from S3, the XRD pattern reveals a 2D phase structure of ZIF-8, also known as ZIF-L with high crystallinity [73], especially with sharp peaks at 2θ of 7.58°, 10.80°, 12.54°, 14.95°, 16.49° and 17.86° [75]. For all the samples, the sharp and narrow peaks are indicative of the favorable crystallinity of the material. The variations in the XRD patterns of the ZIF-8 samples obtained from S1 and S2 upon exposure to CO₂ show that significant structural changes have emerged as a result of the attachment of the gas molecules, supporting the fact that a new arrangement has created and caused the formation of a second configuration composed of a CO₂ molecule within the same crystallographic locations. The detection of the CO₂ species by XRD from the increased intensity indicates the presence of small chemisorbed species that results from chemical bonds such as the $\pi\cdots\pi$ interaction between CO₂ and aromatic rings of the linker [76]. As for the ZIF-8 sample obtained from S3, there is no notable difference in the XRD patterns after exposure to CO₂ which can indicate that the CO₂ species are only physisorbed [77]. In the ZIF-8 and ZIF-L cages, the diameter of the six-membered ring's aperture where the methyl groups of the linker are pointing to the center allows the diffusion of CO₂ into the pores. The physisorbed interactions occur by the favorable electrostatic adsorption sites which are located on both edges of six-ring channel and in the center of the available surface area

near to the aromatic rings, in addition to the Van der Waals interactions that are high in the sodalite cage [78].

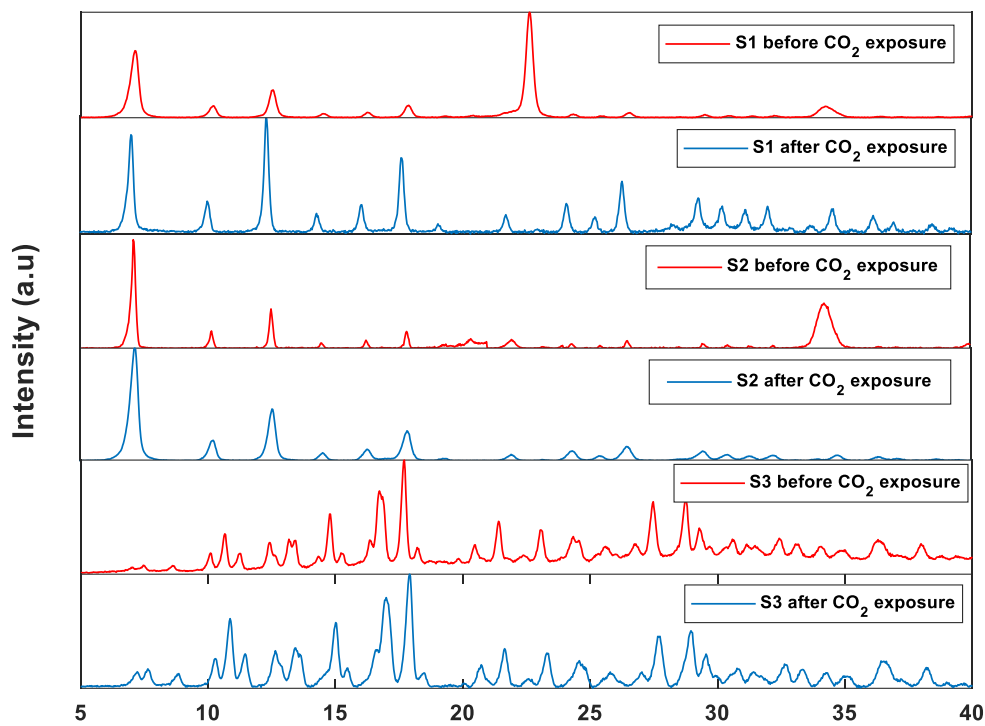


Figure 4-1: XRD patterns for S1, S2, and S3 MOFs before and after CO₂ exposure.

4.1.2. FE-SEM/EDS analysis

Figure 4-2 shows the FE-SEM images obtained for the different ZIF-8 samples. The synthesis approach worked because the ZIF-8 crystals resulted from the S1 and S2 synthesis had rhombic dodecahedron morphologies, which is in agreement with the results found in literature [72]. On the other hand, the ZIF-L 2D phase obtained from S3 had a closer morphology to a cruciate flower, which also confirms the results found in [73]. It can also be observed that there is no major difference in the morphology after adsorption of CO₂. The EDS color map in Figure 4-3 shows the elemental composition of each sample before and after CO₂ exposure. The mapping revealed that the C, Zn, and N elements were distributed uniformly on the surface of the MOFs. The O element could be obtained from the zinc nitrate hexahydrate residue or the conductive sticky substrate employed in the characterization [72]. There's a very limited increase in the

percentage of C in all the samples after exposure to CO₂, however, it can still confirm the CO₂ capture.

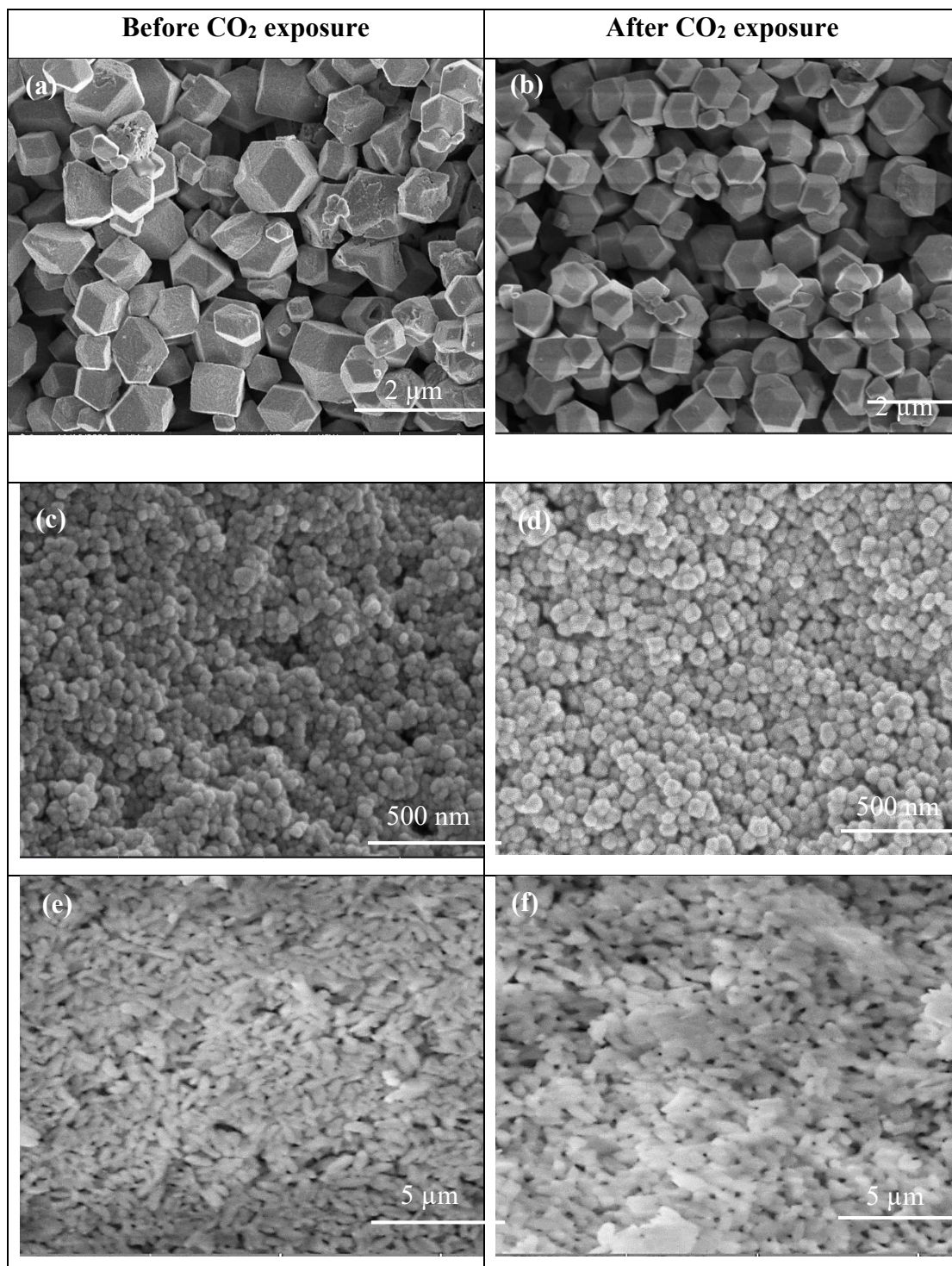


Figure 4-2: FE-SEM for ZIF-8 synthesized using S1, S2 and S3 before and after exposure to CO₂.

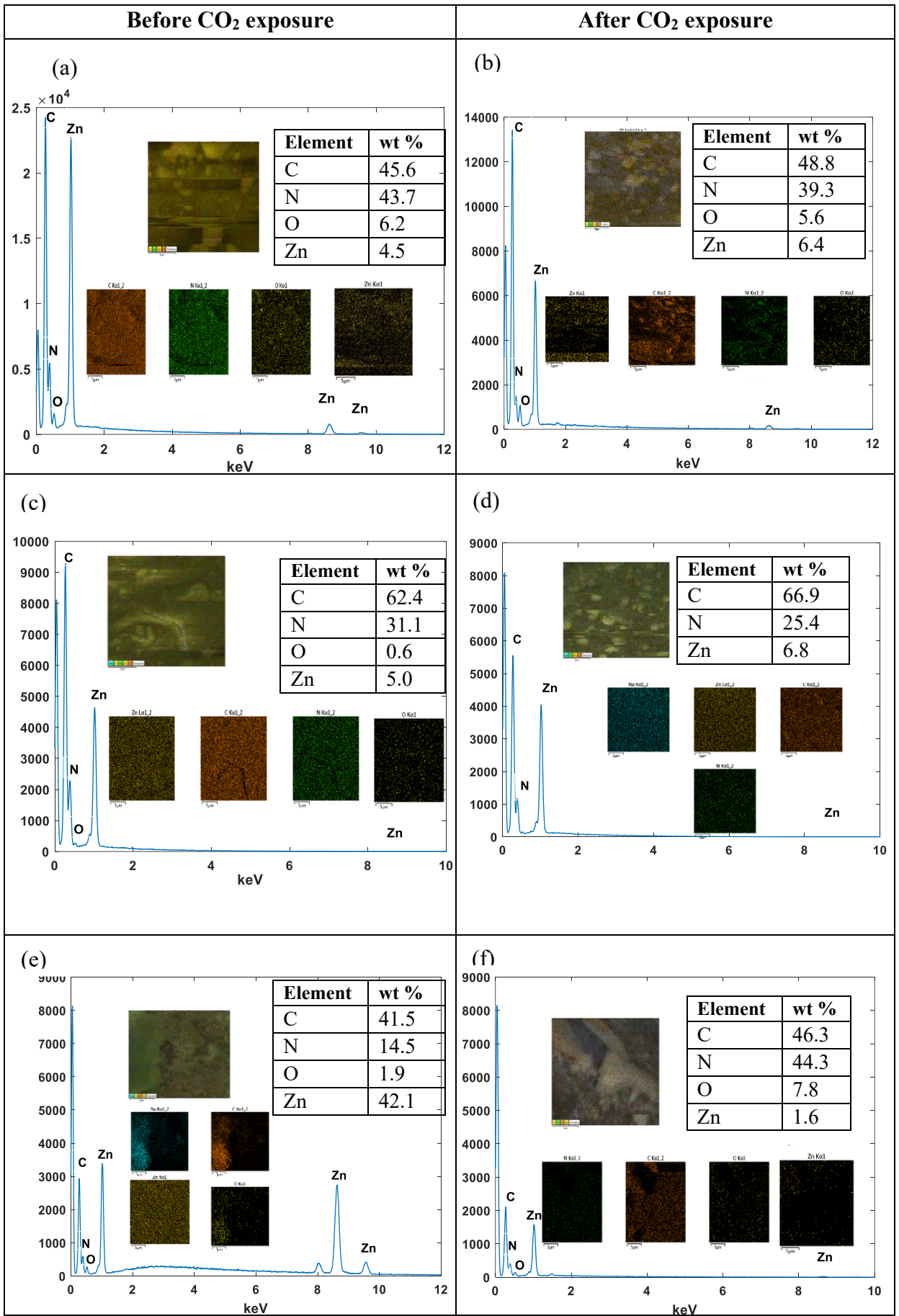


Figure 4-3: EDS color map of (a) S1 ZIF-8 before and (b) after, (c) S2 ZIF-8 before and (d) after, (e) S3 ZIF-8 before and (f) after CO₂ exposure.

4.1.3. FTIR spectroscopy analysis

Figure 4-4 displays the Fourier transform infrared (FTIR) spectra of the ZIF-8 samples. The FTIR results demonstrates that ZIF-8 successfully incorporated amino groups. For the ZIF-8 samples (S1 and S2), notable bands are obtained at 2929, 1458, 1425, 1385, 1309, 1146, 995, 760, 694, and 426 cm^{-1} . These FT-IR bands are in close agreement with those previously reported in [18],[19].

For the ZIF-L phase (S3 sample), the following peak designations are made: 1570 cm^{-1} , C= N stretching; 755 cm^{-1} , Zn–O imidazole ring bending; 674 cm^{-1} , Zn–N imidazole ring bending. The spectrum after adsorption of CO₂ not only confirms the storage of CO₂, but it also offers compelling proof of CO₂ and ZIF-8 framework interactions. For example, the 1146 cm^{-1} generated from the aromatic C-N stretching mode, shows a sharper peak after adsorption of CO₂ in ZIF-8. Also, the bands between 1707 and 1366 cm^{-1} increased slightly due to the chemisorbed CO₂ in the ZIF-8 samples [77]. This is as opposed to the ZIF-L phase in which the peaks did not increase.

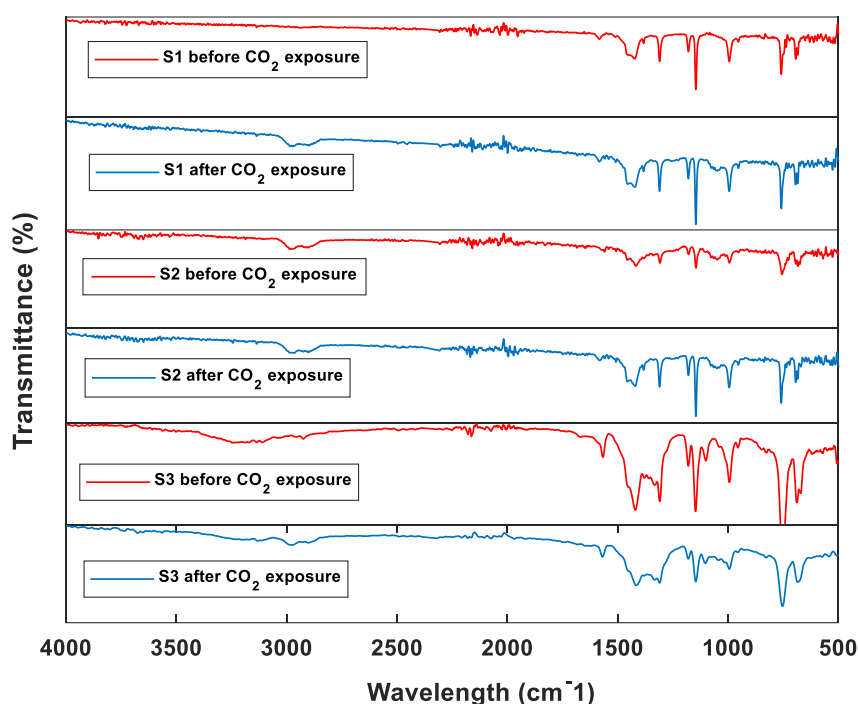
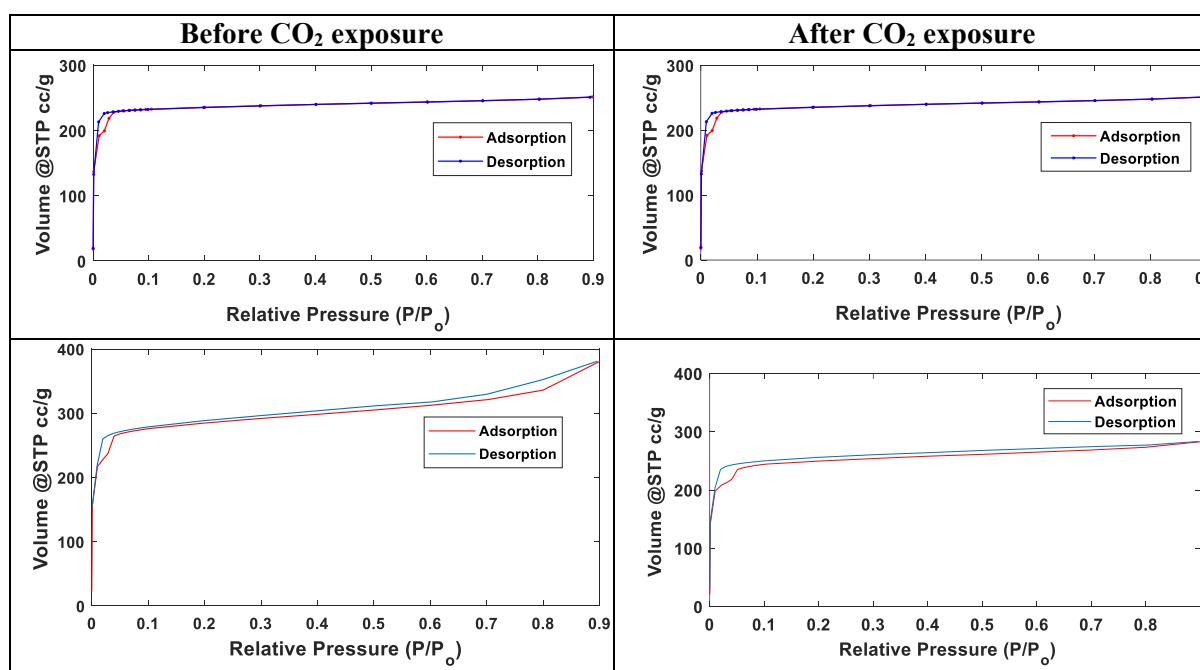


Figure 4-4: FT-IR spectra for ZIF-8 samples before and after CO₂ exposure.

4.1.4. BET analysis

The N₂ adsorption-desorption isotherms for the ZIF-8 samples are shown in Figures 4-5 at 77 K. The ZIF-8 samples produced from the S1 and S2 synthesis obviously exhibited type I isotherm behavior, indicating that they are micropores. These results are consistent with previously reported ZIF-8 isotherms [18]. Furthermore, at low (P/P₀) pressures, the adsorbed nitrogen in all samples rises steadily, indicating the presence of micropores. On the other hand, the isotherm of ZIF-L sample obtained from S3 indicates type IV behavior. It constitutes then a mesopores material. Furthermore, the produced isotherms showed a hysteresis loop when approaching P/P₀ = 1. This demonstrates the existence of interfacial mesoporosity and macroporosity between MOF particles. The results are in agreement with the findings reported in [18],[19]. The Brunauer–Emmett–Teller (BET) surface area, pore volume, and pore diameters are shown in Table 4-1 before and after CO₂ exposure. It is clear that the ZIF-8 samples obtained following S1 and S2 have much higher surface area and pore volume compared to the S3 sample. The very small reduction in both the surface area and the pore volume after exposure to CO₂ can prove the existence of CO₂ molecules within the material [79]. Comparing to the CO₂ molecular diameter of 3.34 Å [80], the S1 and S2 pore sizes are around 10.762 Å, while the S3 pore size is around 17.656 Å before exposure and increased to 27.69 Å after exposure due to CO₂ adsorption.



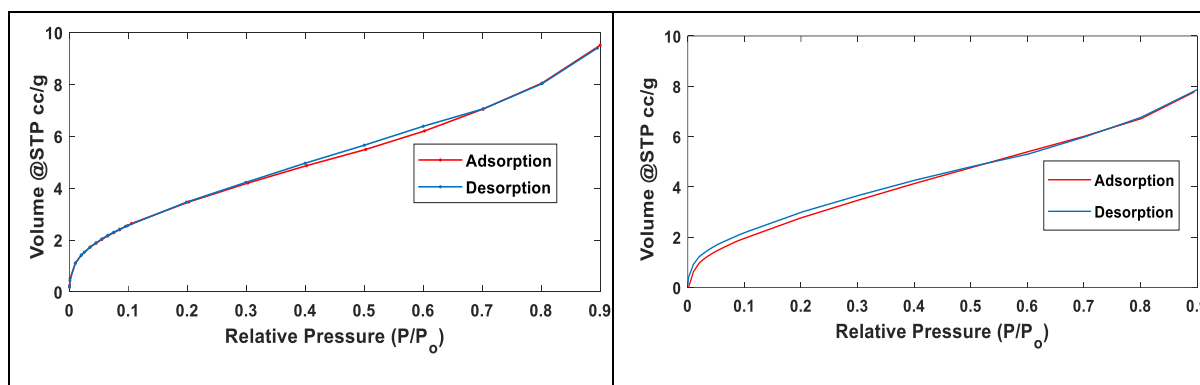


Figure 4-5: Adsorption isotherms of ZIF-8 synthesized using S1, S2 and S3, respectively, before and after exposure to CO₂.

Table 4-1: Surface area and pore volume for the 3 samples before and after CO₂ adsorption.

Type	Experiment (before/after CO ₂)	BET surface area (m ² /g)	Pore volume (cc/g)	Pore size (Å)
S1	Before	1084.614	0.373	10.762
	After	974.539	0.343	10.762
S2	Before	1136.505	0.527	10.762
	After	985.471	0.389	10.762
S3	Before	13.974	0.013	17.656
	After	12.199	0.011	27.69

4.1.5. TGA analysis

We show in Figure 4-6 the TGA results in terms of the variations of the mass percentage with the temperature. The results demonstrate and compare the thermal stability of all synthesized ZIF-8 samples. Furthermore, the observed trends are in close agreement with those obtained in [81]. For the S1 synthesized ZIF-8 (see Figure 4-6(a)), an initial weight loss of about 4 % that occurred at about 200 °C, is mainly due to the methanol solvent evaporation. When reaching 400 °C, the greatest weight loss is observed. There was a 67 % weight loss that is mainly caused by the loss of organic linker molecules, leading to the destruction of the framework and the loss of certain species from the nanocrystals [82]. The TGA pattern of the S2 ZIF-8 (see Figure 4-6(b)) showed that higher temperatures are needed for degradation, and thus, indicates a higher thermal stability. The initial reduction of 14% occurred due to evaporation of trapped solvent, which was also methanol. This is followed by about 66% of weight loss around 600 °C which results from the thermal decomposition of the MOF and organic linker dissociation.

As shown in Figure 4-6(c), the TGA results of S3 synthesized ZIF-8 which corresponds to ZIF-L show a slightly different trend from that of ZIF-8 obtained from S1 and S2. The weight loss occurs in two stages. In the first stage, the moisture evaporates at a temperature of around 50°C. At around 180 °C the reduction is due to the loss of residual linker. A weight loss of ~22 % with steeper slope initiates at 150°C and continues until 300°C. Beyond this temperature, the TGA curve shows a dramatic weight loss of about 56 % until reaching a temperature of 700 °C. This is caused by the thermal decomposition of ZIF-8, producing ZnO as the final decomposition byproduct of the nanocrystals. The TGA results demonstrate that the MOF structure was maintained in the ZIF-8 produced using the solvent-free technique up to 300 °C.

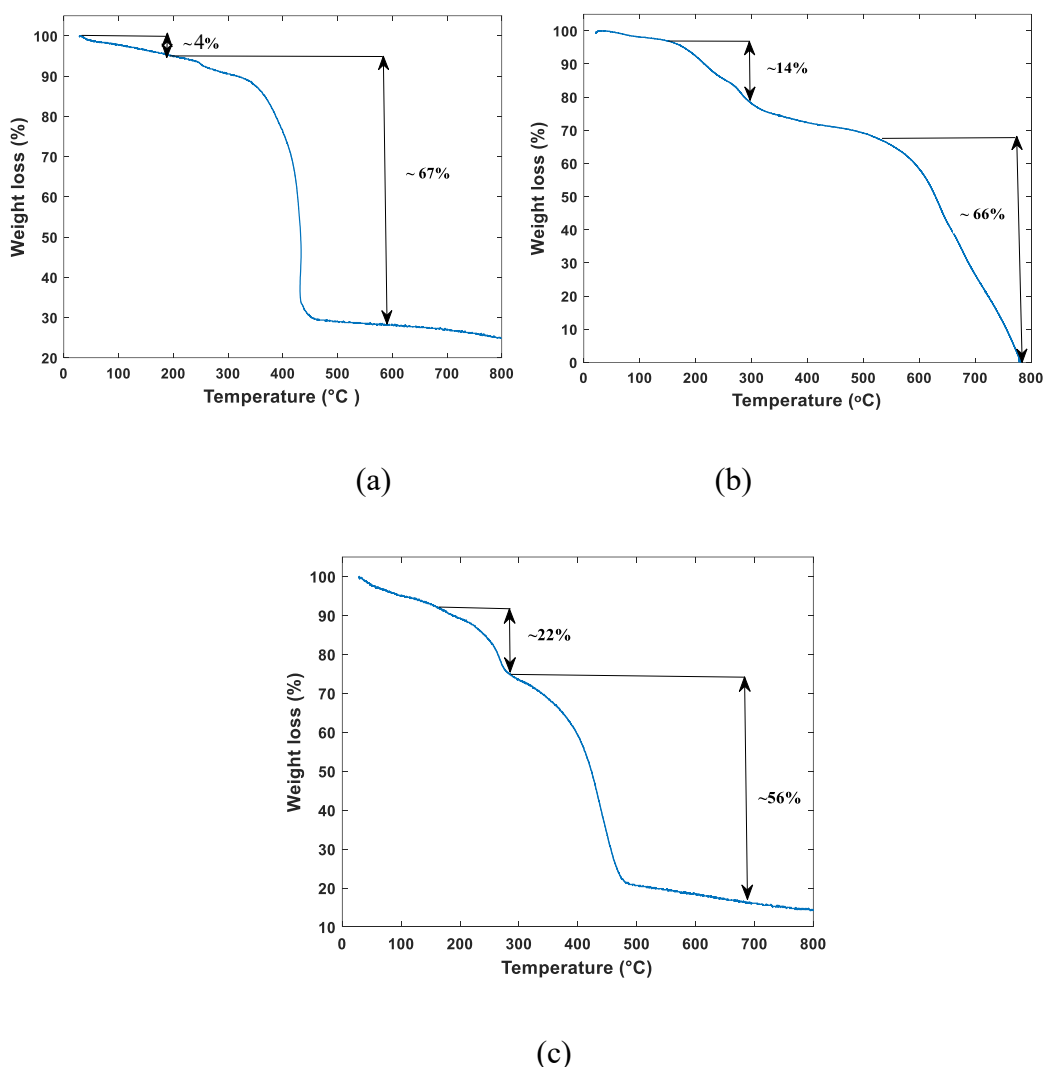


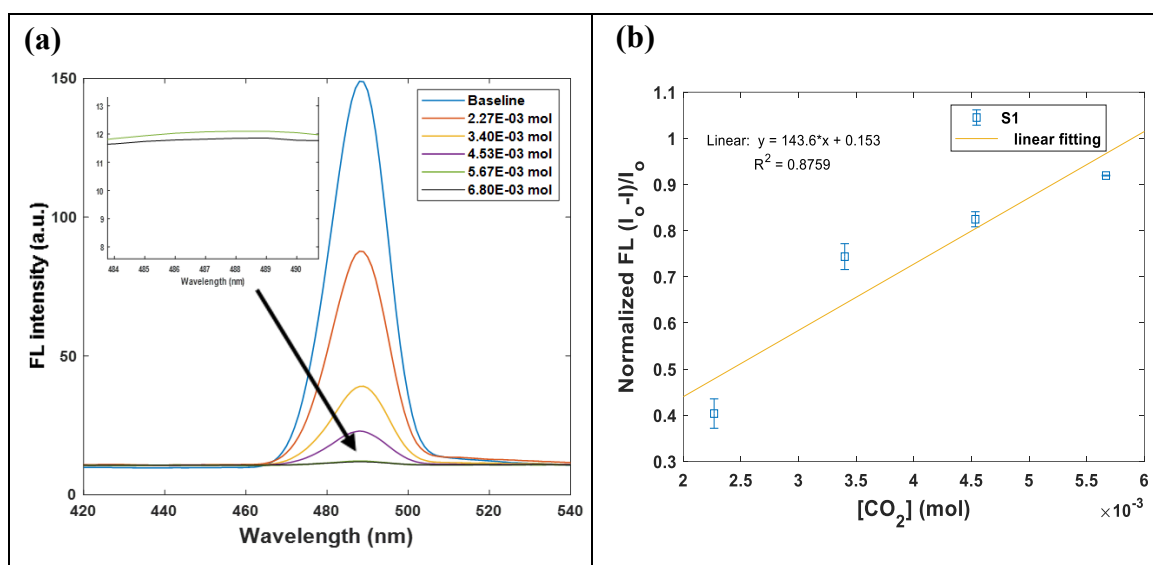
Figure 4-6: TGA results showing the greatest weight loss of (a) S1 stating at 400 °C, (b) S2 at 600 °C, and (c) S3 at 400 °C.

4.2. CO₂ Detection Tests

To assess the capability of ZIF-8 to detect CO₂, the response of the MOFs toward CO₂ is examined using the fluorescence method, as described in the previous section. The fluorescence materials have gained high interest in scientific investigations given their various prospective applications including sensing [83]. Figure 4-7 shows the fluorescence intensity as function of the wavelength and the normalized intensity as function of the CO₂ concentration. The results are obtained based on the fluorescence measurements conducted on the ZIF-8 samples produced from S1, S2 and S3 synthesis techniques. For the samples obtained from S3 and S1, a reduction in intensity is observed after bubbling the CO₂ which indicates that the MOF exhibited a turn-off response, also known as quenching. There was a significant fluorescence quenching in the S3 sample after the injection of CO₂. The fluorescence intensity reduces dramatically from the baseline after bubbling with the highest gas concentration. This results in a quenching percentage of 93.42 %. The fluorescence intensity reduces as the concentration of the injected CO₂ increases until reaching saturation of 12.19 a.u. at a CO₂ concentration of 5.67×10^{-3} mol. This rapid and intense quenching reveals the capability of ZIF-8 to detect the CO₂ gas. The fluorescence level can be used as an indicator of the presence of CO₂ and the associated concentration can be extracted from the fluorescence intensity. Moreover, the considerable reduction in the peak indicates that the CO₂ adsorption mechanism has a significant impact on the MOF luminescence characteristic, and the adsorption of the CO₂ molecules results in a major modification in the MOF structure. In these MOFs, the luminescence is dependent on the luminescence of the linker (2-methylimidazole), which is related to the π – interactions [84]. Since the most highly adsorptive sites for CO₂ in ZIF-8 and ZIF-L are those near the imidazole rings, the fluorescence is quenched upon interaction with CO₂ [78]. Another factor causing the quenching is the collisions due to interactions with the gas molecules which causes the deactivation of the MOFs [83]. On the other hand, for the S2 samples, the MOF was turned on as the intensity was increasing until reaching saturation point. The turn-on phenomenon can be attributed to the ZIF-8's larger pore size in this sample and the desirable molecular physical interactions between CO₂ and the surface. This high capacity is most likely a result of the MOF's high crystallinity, surface area and micropore volume. All of these factors contributed to adsorption of the electrophile CO₂ via bonding with the metal sites [85]. The aggregation that occurs due

to the restriction of the rotating organic groups' molecular motion upon activation is mostly the driving force for fluorescence enhancement [83]. The fluorescence characteristics of materials are influenced by the synthesis process and morphology. Fluorescent materials' properties can be intensified or diminished due to changes in bonding, energy, or electron transport methods when they interact with other molecules [83].

The linear relationship of the fluorescence intensity to CO₂ is found from 1.70×10^{-3} mol to 4.53×10^{-3} mol for the S3 (Figure 4-7 (f)) and S2 samples (Figure 4-7 (d)), and 2.27×10^{-3} to 5.67×10^{-3} mol in the S1 sample (Figure 4-7 (b)). Also, there is a strong linear correlation in the plot of fluorescence intensity against CO₂ concentration in which the R^2 values were 0.8759, 0.9692, and 0.9613, for S1, S2 and S3 samples, respectively. The CO₂ adsorption occurs in the MOFs due to the high electronegativity of the functional groups [86]. Also, the open metal site displays a considerable interaction with CO₂ as a result to an electrophile of CO₂ [87].



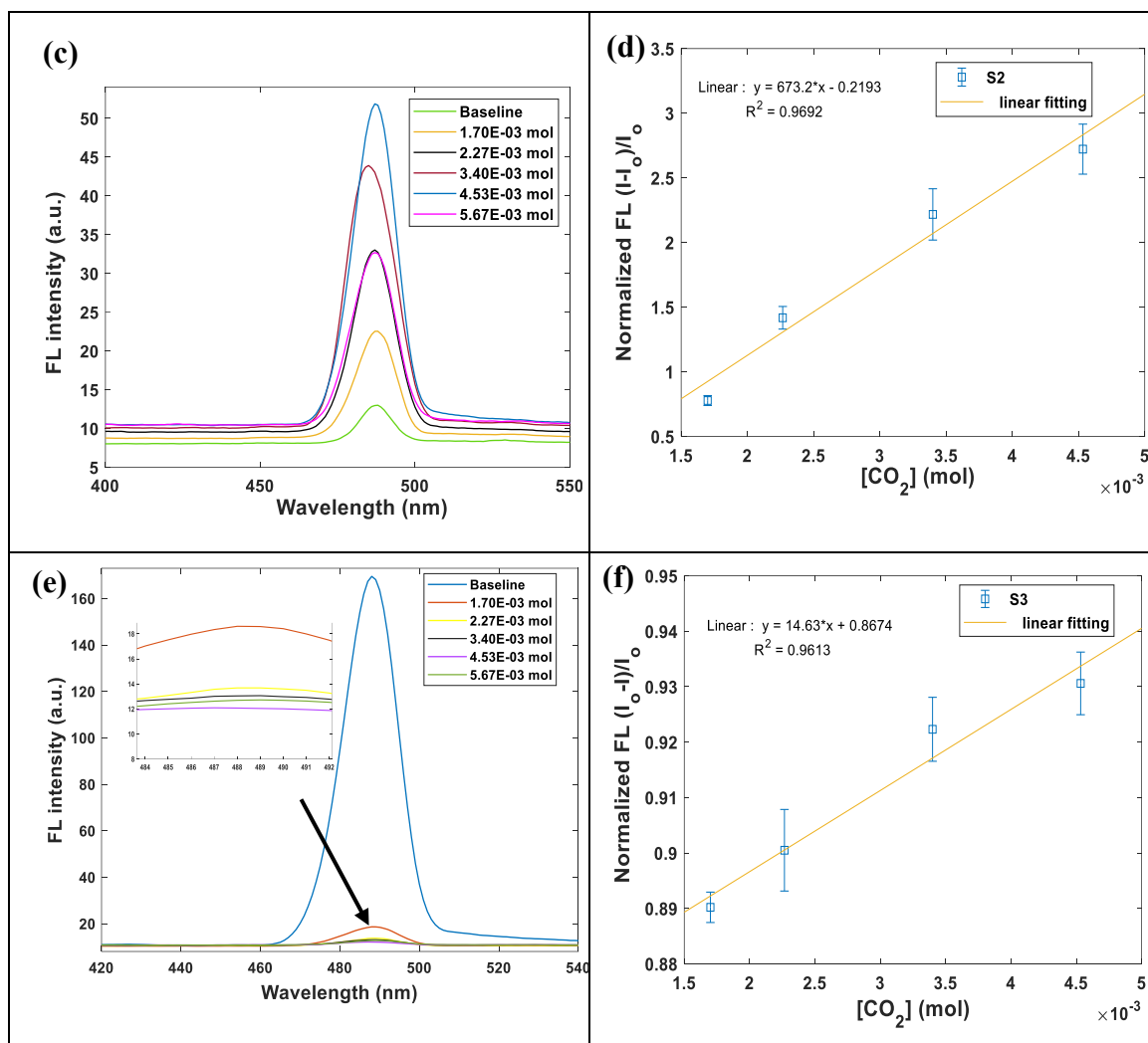


Figure 4-7: Fluorescence intensity and Normalized Fluorescence of the (a)-(b) S1, (c)-(d) S2 and (e)-(f) S3 ZIF-8 with different CO₂ concentrations. Points represent the average of three trials and error bars represent the standard deviation of three trials.

The limit of detection was calculated using the calibration curve shown in Figures 4-7 (b), (c) and (f). The linear equation was obtained by plotting the normalized fluorescence intensity (i.e. $\frac{I_0 - I}{I_0}$, where I and I_0 represent the fluorescence intensity with and without exposure to the analyte, respectively [88]) versus the concentration of CO₂. Furthermore, LOD was obtained using equation 2 below:

$$\text{LOD} = \frac{3\sigma}{s} \quad (2)$$

where σ and s are the standard deviation of the baseline and the slope of the calibration curve (shown in Figure 4-7 (b), (d) and (f)), respectively [89]. The S2 ZIF-8 shows the lowest limit of detection (723.8 ppm at 25 °C) while the S1 ZIF-8 sample yields the

highest value of LOD (1780.6 ppm). This might be attributed to the use of a vacuum oven at room temperature for obtaining the resultant MOF which caused high crystallinity of the material. This was also observed in the XRD patterns where the main peaks related to the crystallinity of the material were higher for the S2 MOF and then, leading to an improvement in its CO₂ detection capability. The S3 MOF shows a good potential for CO₂ detection given the obtained LOD value of 815.2 ppm, and hence, proves the validity of the ZIF-L for CO₂ detection. In a previous study by [66], ZIF-8 was synthesized using the solvothermal technique and resulted in a LOD of 3130 ppm at room temperature and 774 ppm at 4.85 °C. The applications where our synthesized MOFs could be utilized are in indoor buildings at room temperature in addition to the industrial processes. Buildings typically have indoor air with a CO₂ concentration between 350 and 2500 ppm, according to ANSES [90]. Another study, dealing with benzene and CO₂ detection at room temperature, reported a sensor consisting of MOF films produced on-chip on Pt interdigitated electrodes using a solvothermal technique. The LOD of the adjusted Mg-MOF-74 tested for CO₂ detection was found equal to 200 ppm [35]. According to a new study by Lee et al. [89], revealed that under optimal conditions, the LOD calculated for PVIIm-NH₂ based chemosensor was 110 ppm.

Next, we examine the selectivity of the S3 MOF sample (ZIF-L) by inspecting the quenching of its fluorescence intensity when exposed to different gases, including N₂, Ar, and air. The selectivity results under room temperature are shown in Figure 4-8. The results demonstrate that ZIF-L is more selective to CO₂. The ratio I/I_0 where I is the intensity obtained after exposing the CO₂ with a concentration of 0.15 L/min to the MOF for 20 s and I_0 is the baseline intensity reaches 18.34 %. Larger values of the ratio I/I_0 are obtained for N₂, Ar, and air. Clearly, ZIF-L is much less sensitive to air. This is desired for applications where other competing gases exist. In the study of Chocarro-Ruiz et al. [66], a high selectivity over N₂ was obtained at low temperature. Since ZIF-L features a 9.4 °A × 7.0 °A × 5.3 °A cushion-shaped hollow between the layers that can accommodate CO₂ molecules. Similarly, the imidazole functional group on ZIF-L particles can interact strongly with CO₂ [91].

The quenching-recovery cycles were performed to test the recyclability of the S3 MOF sample. The corresponding results in terms of changes in the fluorescence intensity are shown in Figure 4-9. After exposing it to CO₂, the fluorescence recovery is observed

by bubbling N_2 and then the fluorescence quenching is observed again when exposing it again to CO_2 in which the MOF is able to regenerate. However, after the second cycle, the MOF lost its ability to regenerate most probably due to its degradation in water [92].

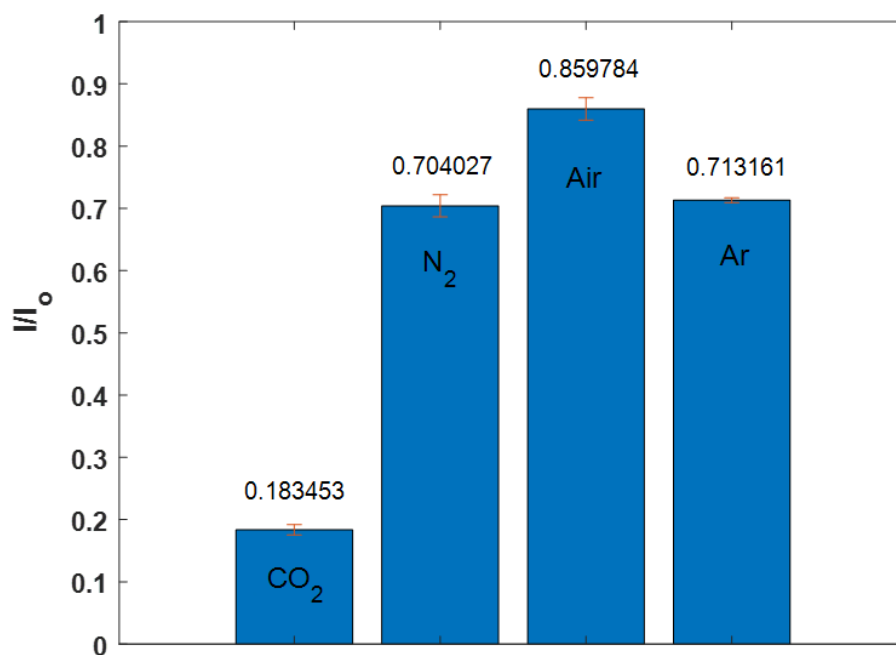


Figure 4-8: Selectivity results of S3 MOF when exposed to CO_2 and other gases.

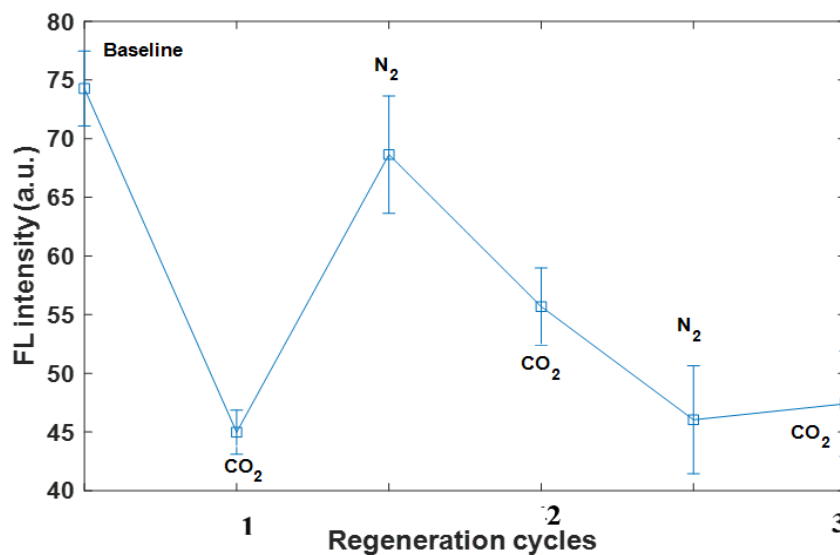


Figure 4-9: Changes in the fluorescence intensity of the ZIF-8 (S3) upon exposure to CO_2 over three cycles.

The noticeable change in brightness when exposing ZIF-8 or any of its variants to CO₂ can be exploited to quantify the CO₂ concentration using hardware and software tools. The fluorescence intensity of sensing materials can be increased, quenched, or changed in color, and thus can be used for optical sensing devices. A high surface-volume ratio, which enables the detection of a low levels of target analytes, is a factor contributing to the advantages of utilizing optical nanoparticles [83]. The visual fluorescence color variation of the solution using UV light irradiation (365 nm), as shown in Figure 4-10, clearly demonstrates the quenching phenomenon when increasing the flow rates of CO₂ from 0.15 L/min (1.70×10^{-3} mol) until 0.7 L/min (7.93×10^{-3} mol). The last two cases also show the complete saturation of the MOFs. It is also worth noting that the change occurs immediately upon bubbling the CO₂.

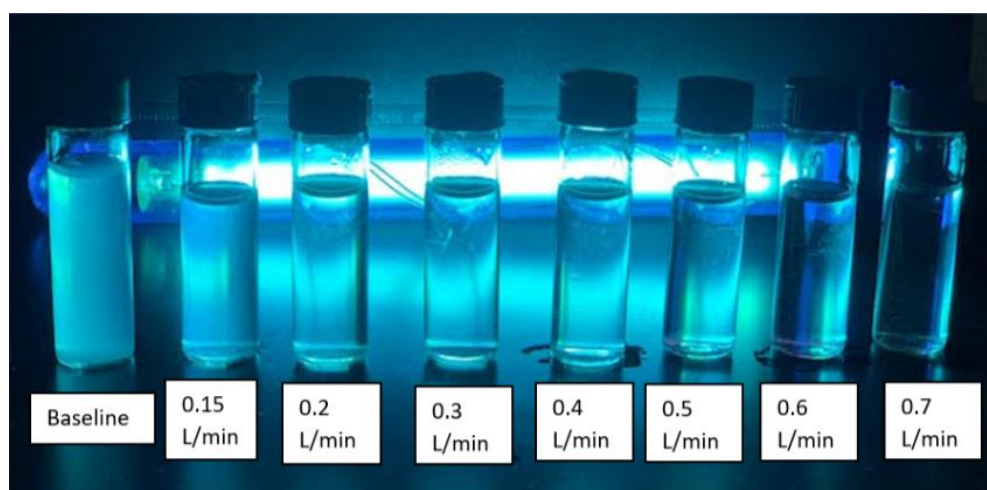


Figure 4-10: MOFs' turn-off in the water after being bubbled with CO₂ at different concentrations and exposed to UV light.

4.3. Coated Substrate Results

4.3.1. SEM/EDS results

Figure 4-11 demonstrates the alterations in the surface morphology of the carbon fibers when subjected to different milling speeds. As illustrated in Figure 4-11 (a), the surface of the undeposited carbon fibers was smooth compared to the other deposited carbon fibers. These findings are in line with previous SEM images reported in the literature [93]. The different deposition of ZIF-8 on the fibers in Figures 4-11 (b), (c) and (d), is caused from the milling speeds considered in the present study: 100 rpm, 300 rpm and

500 rpm. The results revealed a dense stacked rhombic dodecahedron nanoparticles with more MOF particles deposited on the substrate coated using the 300 rpm speed (Figure 4-11 (c)), which was also observed previously in the images taken after deposition in Chapter 3 (Figure 3-3). However, inspecting Figure 4-11 (d), we noticed that the higher milling speed of 500 rpm did not lead to a better deposition. The EDS color map in Figure 4-12 shows the elemental composition of each substrate after exposure to CO₂. From the spectra, only C was detected on the surface of the carbon cloth (without CO₂ exposure) in Figure 4-12 (a) which is in agreement with previously published data [94]. The mapping indicated the uniform distribution of C, Zn, and N elements on the surface of the coated carbon fibers, as seen in Figure 4-12 (b), (c) and (d), with low percentage of O. Also, less C element is found in Coating 3 (obtained at a milling speed of 500 rpm) compared to Coating 2 which indicates that the substrate is not superior for CO₂ capture. The higher C element indicates an increase in CO₂ on the substrate [95]. The EDS results show values close to that obtained by Lipei et al. [96], in which the ZIF-8 was deposited on an activated carbon fiber (ACF) felts using atomic layer deposition method. The ball milling technique is found to be rapid, simple, and expandable for producing MOF deposition instantly on non-prefunctionalized flexible substrates, with outstanding reliability and functionality compared to hydrothermally fabricated coatings [97].

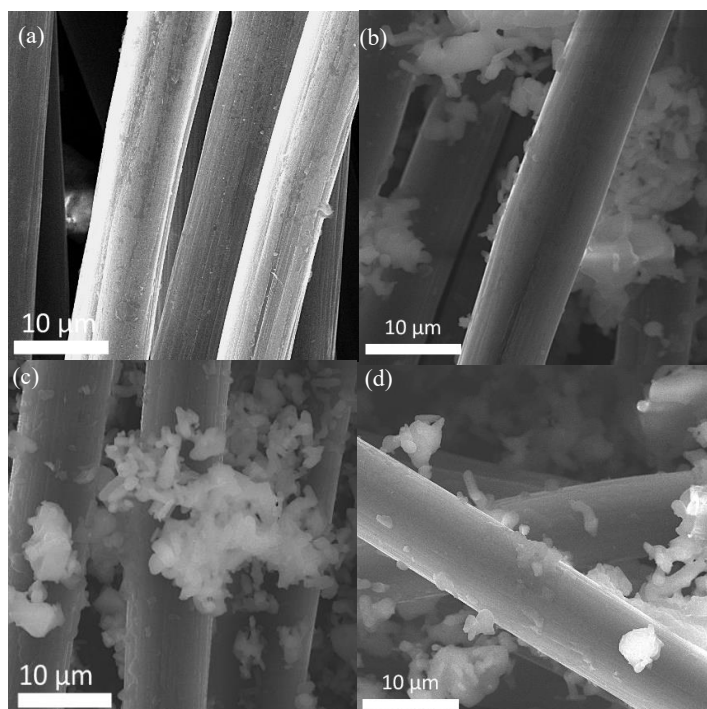


Figure 4-11: SEM images of (a) carbon cloth sample, (b) the coated sample using 100 rpm, (c) 300 rpm, and (d) 500 rpm milling speeds.

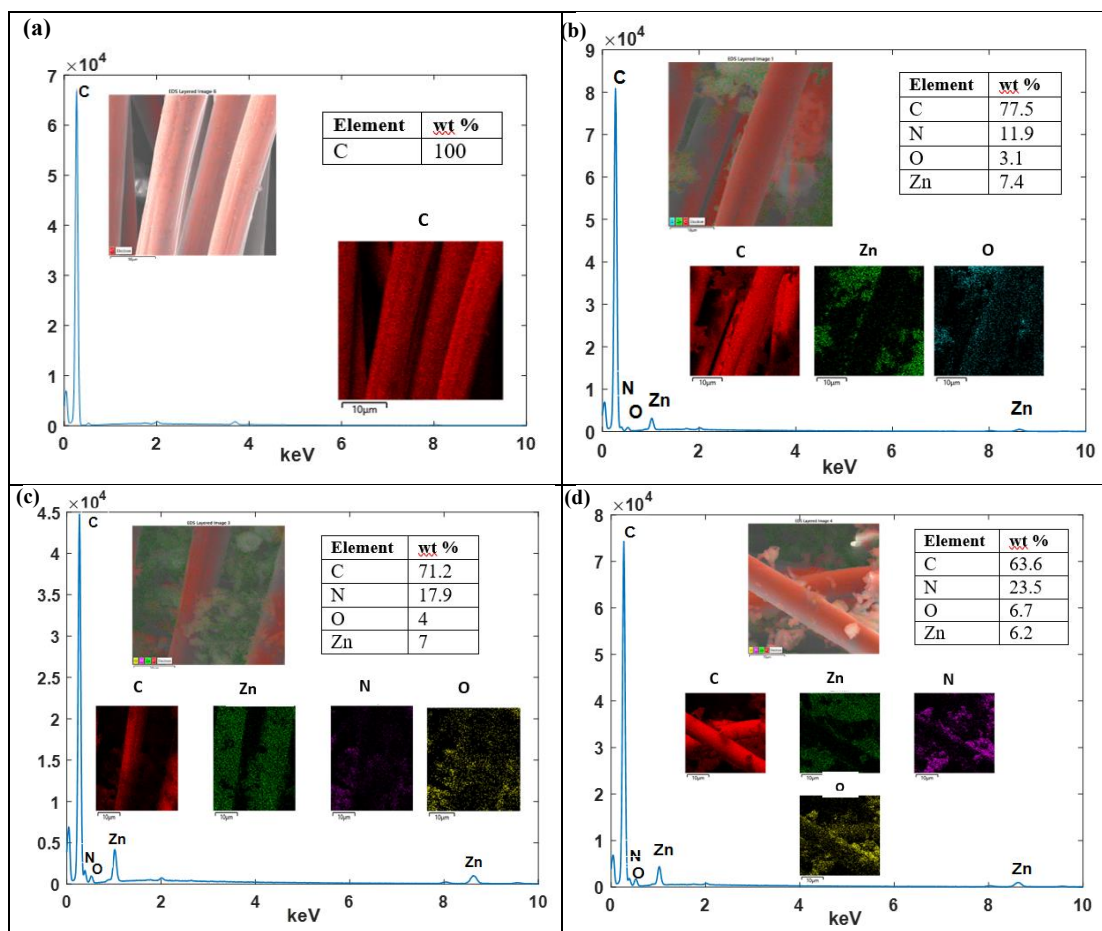


Figure 4-12: EDS color map of (a) carbon cloth sample, (b) the coated sample using 100 rpm, (c) 300 rpm, and (d) 500 rpm milling speeds.

4.3.2. Gas chromatography results

Figure 4-13 shows the concentration of carbon dioxide in mole % averaged based on repeated measurements for four samples including a control sample and three coated substrates with different ball milling speeds (100 rpm, 300 rpm, and 500 rpm), referred to as Coating 1, Coating 2 and Coating 3, respectively. The short error bars demonstrate the repeatability of the experimental measurements. According to the results, the sample taken from the control sample vial had a CO₂ concentration of ~ 45.25 %, whereas the sample taken from Coating 1 vial showed a slight reduction in concentration to around ~44.16% with a CO₂ reduction percentage of 2.4%. This could be attributed to the low rotational speed which can result in less material coated on the substrate. In Coating 2, a significant reduction in concentration was achieved (~ 21.06

%) with a reduction percentage of 53.46 %, indicating that higher MOF particles were deposited and caused higher adsorption of CO₂. Lastly, for Coating 3, the observed concentration of the gas was ~23.46 %. The high rotational speed of 500 rpm did not lead to a better deposition compared to Coating 2 as excess of energy was applied which subsequently affected the CO₂ adsorption. Thus, we can conclude that the optimal coating was achieved at a milling speed of 300 rpm. This could also be implemented for CO₂ sensing applications in which the low concentrations of CO₂ can be adsorbed instantly by the coated substrate.

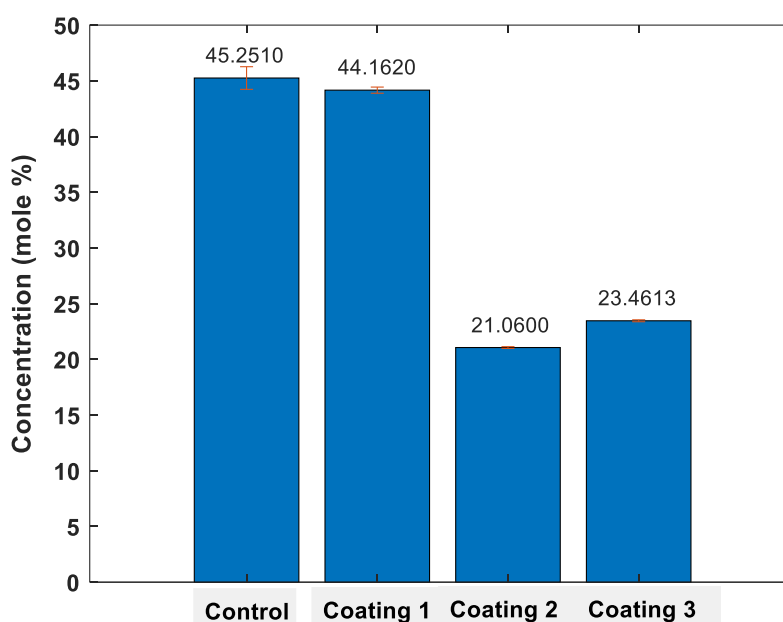


Figure 4-13: Gas chromatography CO₂ concentration in the test vials for coated ZIF-8 sample at different ball milling speeds and uncoated carbon cloth substrates.

Chapter 5. Conclusion and Future Work

In this thesis, we demonstrated the capability of the MOF ZIF-L synthesized by the ball milling technique to detect CO₂ gas with an LOD of 815.2 ppm, in addition to its high selectivity over other gases, such as N₂, Ar, and air, at room temperature and good recyclability. Furthermore, the performance of the MOFs obtained from other synthesis techniques in terms of CO₂ detection was examined. The room temperature synthesized MOF showed a lower LOD than the ZIF-L phase. The XRD characterizations showed the physisorption and chemisorption interactions with CO₂. The FTIR, FE-SEM and EDS tests revealed the differences in morphology and structure between the ZIF-8 and ZIF-L phase, before and after exposure to CO₂. The BET analysis showed the reduction in the pore size of the MOFs upon CO₂ adsorption. The TGA results illustrated the thermal stability of the three samples. Lastly, the coating on carbon cloth substrates showed the success of deposition for detecting CO₂ at an optimal milling speed of 300 rpm. The findings demonstrate the following two important points:

- The enormous potential of mechanochemistry to develop an efficient and solvent-free MOF synthesis and deposition.
- The necessity of further research into continuous, higher-scale mechanochemical processes, in order to increase the effectiveness and sustainability of the process.

The benefit of the applied dry MOF synthesis includes avoiding the use of harmful/toxic solvents or chemicals and ionic liquids used in previous studies to assist the reactions while creating more output. As a potential extension of the present work, the sensing layer can be integrated with a MEMS device that detects the changes in mass after the adsorption of the gas analyte. Furthermore, different substrates can be examined in order to investigate the change in the coating structure and thickness. Several chemical processes and environmental topics are involved in CO₂ reduction, storage, and detection. However, few works have been conducted on the application of MOFs for CO₂ detection. The majority of these investigations reported CO₂ sensors, which usually require huge equipment to detect. As a result, we anticipate that more research will be conducted to evaluate the MOFs potential for miniature sensors.

References

- [1] M. Shahnawaz Khan, M. Khalid, and M. Shahid, "What triggers dye adsorption by metal organic frameworks? The current perspectives," *Mater. Adv.*, vol. 1, no. 6, pp. 1575–1601, 2020, doi: 10.1039/d0ma00291g.
- [2] C. Yim, M. Lee, M. Yun, G. H. Kim, K. T. Kim, and S. Jeon, "CO₂-Selective nanoporous metal-organic framework microcantilevers," *Sci. Rep.*, vol. 5, no. 10674, pp. 2045–2322, 2015, doi: 10.1038/srep10674.
- [3] H. Wang *et al.*, "Gas sensing materials roadmap," *Journal of Physics Condensed Matter*. 2021, doi: 10.1088/1361-648X/abf477.
- [4] M. H. Zarifi, A. Gholidoust, M. Abdolrazzagh, P. Shariaty, Z. Hashisho, and M. Daneshmand, "Sensitivity enhancement in planar microwave active-resonator using metal organic framework for CO₂ detection," *Sensors and Actuators, B: Chemical*, vol. 255. pp. 1561–1568, 2018, doi: 10.1016/j.snb.2017.08.169.
- [5] U. Yaqoob and M. I. Younis, "Chemical gas sensors: Recent developments, challenges, and the potential of machine learning—a review," *Sensors*, vol. 21. p. 2877, 2021, doi: 10.3390/s21082877.
- [6] M. Ko, A. Aykanat, M. K. Smith, and K. A. Mirica, "Drawing sensors with ball-milled blends of metal-organic frameworks and graphite," *Sensors (Switzerland)*, vol. 17, no. 10, p. 2192, 2017, doi: 10.3390/s17102192.
- [7] H.-T. Kim, W. Hwang, Y. Liu, and M. Yu, "Ultracompact gas sensor with metal-organic-framework-based differential fiber-optic Fabry-Perot nanocavities," *Opt. Express*, vol. 28, no. 20, pp. 29937–29947, 2020, doi: 10.1364/oe.396146.
- [8] A. S. Algamili *et al.*, "A Review of Actuation and Sensing Mechanisms in MEMS-Based Sensor Devices," *Nanoscale Research Letters*. 2021, doi: 10.1186/s11671-021-03481-7.
- [9] A. Gheorghe, O. Lugier, B. Ye, and S. Tanase, "Metal–organic framework based systems for CO₂ sensing," *Journal of Materials Chemistry C. Royal Society of Chemistry*, pp. 1–11, 2021, doi: 10.1039/d1tc02249k.
- [10] K. Sumida *et al.*, "Carbon dioxide capture in metal-organic frameworks," *Chemical Reviews*, vol. 112. pp. 724–781, 2012, doi: 10.1021/cr2003272.
- [11] X. Chen, R. Behboodan, D. Bagnall, M. Taheri, and N. Nasiri, "Metal-organic-frameworks: Low temperature gas sensing and air quality monitoring," *Chemosensors*, vol. 9. p. 316, 2021, doi: 10.3390/chemosensors9110316.
- [12] Y. Tang *et al.*, "A highly fluorescent post-modified metal organic framework probe for selective, reversible and rapid carbon dioxide detection," *Dyes and Pigments*, vol. 172. p. 107798, 2020, doi: 10.1016/j.dyepig.2019.107798.
- [13] T. V. K. Karthik, L. Martinez, and V. Agarwal, "Porous silicon ZnO/SnO₂ structures for CO₂ detection," *Journal of Alloys and Compounds*, vol. 731. pp. 853–863, 2018, doi: 10.1016/j.jallcom.2017.10.070.

- [14] Y. Zheng, X. Xu, X. Zhang, L. Qin, Y. Lu, and G. Zhang, "Design of Metal-Organic Frameworks with High Lowpressure Adsorption Performance of CO₂," in *IOP Conference Series: Earth and Environmental Science*, 2018, p. 032073, doi: 10.1088/1755-1315/170/3/032073.
- [15] S. Sung and M. P. Suh, "Highly efficient carbon dioxide capture with a porous organic polymer impregnated with polyethylenimine," *Journal of Materials Chemistry A*, vol. 00. pp. 1–3, 2014, doi: 10.1039/c4ta02861a.
- [16] R. Tang, Y. Shi, Z. Hou, and L. Wei, "Carbon nanotube-based chemiresistive sensors," *Sensors (Switzerland)*, vol. 17. p. 882, 2017, doi: 10.3390/s17040882.
- [17] Z. Ahmad, Naseem, S. Manzoor, M. Talib, S. S. Islam, and P. Mishra, "Self-standing MWCNTs based gas sensor for detection of environmental limit of CO₂," *Materials Science and Engineering B: Solid-State Materials for Advanced Technology*, vol. 255. p. 114528, 2020, doi: 10.1016/j.mseb.2020.114528.
- [18] M. Penza, G. Sberveglieri, W. Wlodarski, and Y. Li, "Nanomaterials for Chemical Sensing Technologies," *Journal of Sensors*. 2009, doi: 10.1155/2009/924941.
- [19] H. Bai and G. Shi, "Gas sensors based on conducting polymers," *Sensors*, vol. 7. pp. 267–307, 2007, doi: 10.3390/s7030267.
- [20] C. J. Chiang *et al.*, "In situ fabrication of conducting polymer composite film as a chemical resistive CO₂ gas sensor," *Microelectronic Engineering*, vol. 111. pp. 409–415, 2013, doi: 10.1016/j.mee.2013.04.014.
- [21] Y. C. Wong, B. C. Ang, A. S. M. A. Haseeb, A. A. Baharuddin, and Y. H. Wong, "Review—Conducting Polymers as Chemiresistive Gas Sensing Materials: A Review," *Journal of The Electrochemical Society*, vol. 167. p. 037503, 2020, doi: 10.1149/2.0032003jes.
- [22] X. Liu, W. Zheng, R. Kumar, M. Kumar, and J. Zhang, "Conducting polymer-based nanostructures for gas sensors," *Coordination Chemistry Reviews*, vol. 462. Elsevier B.V., p. 214517, 2022, doi: 10.1016/j.ccr.2022.214517.
- [23] M. J. Vellekoop, "Acoustic wave sensors and their technology," *Ultrasonics*, vol. 36, no. 1–5, pp. 7–14, 1998, doi: 10.1016/S0041-624X(97)00146-7.
- [24] S. Xu *et al.*, "Surface acoustic wave DMMP gas sensor with a porous graphene/PVDF molecularly imprinted sensing membrane," *Micromachines*, vol. 12. p. 552, 2021, doi: 10.3390/mi12050552.
- [25] A. S. Yuwono and P. S. Lammers, "Odour Pollution in the Environment : Development of a Odour Pollution in the Environment :," in *Paper DTT*, 2001, no. December, pp. 1–8.
- [26] B. C. Kaanta, H. Chen, G. Lambertus, W. H. Steinecker, O. Zhdaneev, and X. Zhang, "High sensitivity micro-thermal conductivity detector for gas chromatography," in *Proceedings of the IEEE International Conference on Micro Electro Mechanical Systems (MEMS)*, 2009, pp. 264–267, doi: 10.1109/MEMSYS.2009.4805369.

- [27] A. Mahdaviifar, M. Navaei, P. J. Hesketh, M. Findlay, J. R. Stetter, and G. W. Hunter, “Transient thermal response of micro-thermal conductivity detector (μ TCD) for the identification of gas mixtures: An ultra-fast and low power method,” *Microsystems Nanoeng.*, vol. 1, p. 15025, 2015, doi: 10.1038/micronano.2015.25.
- [28] D. Cruz, J. P. Chang, S. K. Showalter, F. Gelbard, R. P. Manginell, and M. G. Blain, “Microfabricated thermal conductivity detector for the micro-ChemLabTM,” *Sensors Actuators, B Chem.*, vol. 121, pp. 414–422, 2007, doi: 10.1016/j.snb.2006.04.107.
- [29] P. Krebs and A. Grisel, “A low power integrated catalytic gas sensor,” *Sensors Actuators B. Chem.*, vol. 13, no. 1–3, pp. 155–158, 1993, doi: 10.1016/0925-4005(93)85349-F.
- [30] A. Karelin, A. M. Baranov, S. Akbari, S. Mironov, and E. Karpova, “Measurement Algorithm for Determining Unknown Flammable Gas Concentration Based on Temperature Sensitivity of Catalytic Sensor,” *IEEE Sens. J.*, vol. 19, no. 11, pp. 4173–4180, 2019, doi: 10.1109/JSEN.2019.2897626.
- [31] E. Brauns, E. Morsbach, S. Kunz, M. Bäumer, and W. Lang, “A fast and sensitive catalytic gas sensors for hydrogen detection based on stabilized nanoparticles as catalytic layer,” *Sensors and Actuators, B: Chemical*, vol. 193, pp. 895–903, 2014, doi: 10.1016/j.snb.2013.11.048.
- [32] J. Zhang, Z. Qin, D. Zeng, and C. Xie, “Metal-oxide-semiconductor based gas sensors: Screening, preparation, and integration,” *Phys. Chem. Chem. Phys.*, vol. 19, no. 9, pp. 6313–6329, 2017, doi: 10.1039/c6cp07799d.
- [33] F. Sarf, “Metal Oxide Gas Sensors by Nanostructures,” in *Gas Sensors*, 2020.
- [34] S. Y. Bak *et al.*, “Sensitivity improvement of urchin-like ZnO nanostructures using two-dimensional electron gas in MgZno/Zno,” *Sensors (Switzerland)*, vol. 19, no. 23, p. 5195, 2019, doi: 10.3390/s19235195.
- [35] D. J. Wales *et al.*, “Gas sensing using porous materials for automotive applications,” *Chemical Society Reviews*, vol. 44, pp. 4290–4321, 2015, doi: 10.1039/c5cs00040h.
- [36] D. Zhao *et al.*, “Recent Progress in Metal-Organic Framework Based Fluorescent Sensors for Hazardous Materials Detection,” *Molecules*, vol. 27, no. 7, pp. 1–34, 2022, doi: 10.3390/molecules27072226.
- [37] Y. Han, H. Yang, and X. Guo, *Synthesis Methods and Crystallization of MOFs*. 2020.
- [38] N. Stock and S. Biswas, “Synthesis of metal-organic frameworks (MOFs): Routes to various MOF topologies, morphologies, and composites,” *Chem. Rev.*, vol. 112, no. 2, pp. 933–969, 2012, doi: 10.1021/cr200304e.
- [39] R. Zhang, C. A. Tao, R. Chen, L. Wu, X. Zou, and J. Wang, “Ultrafast synthesis of Ni-MOF in one minute by ball milling,” *Nanomaterials*, vol. 8, p. 1067, 2018, doi: 10.3390/NANO8121067.

- [40] A. D. Katsenis *et al.*, “In situ X-ray diffraction monitoring of a mechanochemical reaction reveals a unique topology metal-organic framework,” *Nature Communications*, vol. 6, no. 6662. 2015, doi: 10.1038/ncomms7662.
- [41] T. H. Wei *et al.*, “Rapid mechanochemical encapsulation of biocatalysts into robust metal–organic frameworks,” *Nature Communications*, vol. 10. p. 5002, 2019, doi: 10.1038/s41467-019-12966-0.
- [42] B. Ogunbadejo and S. Al-Zuhair, “MOFs as Potential Matrices in Cyclodextrin Glycosyltransferase Immobilization,” *Molecules*, vol. 26. p. 680, 2021, doi: 10.3390/molecules26030680.
- [43] D. Y. Heo, H. H. Do, S. H. Ahn, and S. Y. Kim, “Metal-organic framework materials for perovskite solar cells,” *Polymers (Basel)*., vol. 12, no. 9, p. 2061, 2020, doi: 10.3390/POLYM12092061.
- [44] A. E. Baumann, D. A. Burns, B. Liu, and V. S. Thoi, “Metal-organic framework functionalization and design strategies for advanced electrochemical energy storage devices,” *Communications Chemistry*, vol. 2, no. 86. 2019, doi: 10.1038/s42004-019-0184-6.
- [45] L. Liang *et al.*, “Carbon dioxide capture and conversion by an acid-base resistant metal-organic framework,” *Nature Communications*, vol. 8, no. 1233. 2017, doi: 10.1038/s41467-017-01166-3.
- [46] J. Khan, N. Iqbal, A. Asghar, and T. Noor, “Novel amine functionalized metal organic framework synthesis for enhanced carbon dioxide capture,” *Materials Research Express*, vol. 6. p. 105539, 2019, doi: 10.1088/2053-1591/ab3ff8.
- [47] N. Y. Huang *et al.*, “Electrostatic Attraction-Driven Assembly of a Metal-Organic Framework with a Photosensitizer Boosts Photocatalytic CO₂ Reduction to CO,” *J. Am. Chem. Soc.*, vol. 143, no. 42, pp. 17424–17430, 2021, doi: 10.1021/jacs.1c05839.
- [48] S. Yuan *et al.*, “Stable Metal–Organic Frameworks: Design, Synthesis, and Applications,” *Adv. Mater.*, vol. 30, no. 37, p. 1704303, 2018, doi: 10.1002/adma.201704303.
- [49] J. H. Deng *et al.*, “ Π - π stacking interactions: Non-negligible forces for stabilizing porous supramolecular frameworks,” *Science Advances*, vol. 6, no. 2. 2020, doi: 10.1126/sciadv.aax9976.
- [50] H. M. Lee, I. S. Youn, M. Saleh, J. W. Lee, and K. S. Kim, “Interactions of CO₂ with various functional molecules,” *Physical Chemistry Chemical Physics*, vol. 17. pp. 10925--10933, 2015, doi: 10.1039/c5cp00673b.
- [51] P. N. Khanh and N. T. Trung, “Understanding Interaction Capacity of CO₂ with Organic Compounds at Molecular Level: A Theoretical Approach,” in *Carbon Dioxide Chemistry, Capture and Oil Recovery*, 2018, p. 105.
- [52] M. Fakhraei Ghazvini, M. Vahedi, S. Najafi Nobar, and F. Sabouri, “Investigation of the MOF adsorbents and the gas adsorptive separation mechanisms,” *J. Environ. Chem. Eng.*, vol. 9, no. 1, p. 104790, 2021, doi: 10.1016/j.jece.2020.104790.

- [53] Y. Belmabkhout, V. Guillerm, and M. Eddaoudi, “Low concentration CO₂ capture using physical adsorbents: Are metal-organic frameworks becoming the new benchmark materials?,” *Chemical Engineering Journal*, vol. 296. pp. 386–397, 2016, doi: 10.1016/j.cej.2016.03.124.
- [54] H. R. Abid *et al.*, “Boosting CO₂ adsorption and selectivity in metal-organic frameworks of MIL-96(Al): Via second metal Ca coordination,” *RSC Advances*, vol. 10. pp. 8130–8139, 2020, doi: 10.1039/d0ra00305k.
- [55] I. Strauss *et al.*, “Metal-Organic Framework Co-MOF-74-Based Host-Guest Composites for Resistive Gas Sensing,” *ACS Applied Materials and Interfaces*, vol. 11. p. 14175–14181, 2019, doi: 10.1021/acsami.8b22002.
- [56] B. Ye, A. Gheorghe, R. Van Hal, M. Zevenbergen, and S. Tanase, “CO₂ sensing under ambient conditions using metal-organic frameworks,” *Mol. Syst. Des. Eng.*, vol. 5, no. 6, pp. 1071–1076, 2020, doi: 10.1039/d0me00004c.
- [57] X. S. Xing, Z. H. Fu, N. N. Zhang, X. Q. Yu, M. S. Wang, and G. C. Guo, “High proton conduction in an excellent water-stable gadolinium metal-organic framework,” *Chemical Communications*, vol. 55. pp. 1241–1244, 2019, doi: 10.1039/c8cc08700h.
- [58] W.-T. Koo, J.-S. Jang, and I.-D. Kim, “Metal-Organic Frameworks for Chemiresistive Sensors,” *Chem*, vol. 5, no. 8, pp. 1938–1963, 2019, doi: 10.1016/j.chempr.2019.04.013.
- [59] L. Yang *et al.*, “Anion Pillared Metal-Organic Framework Embedded with Molecular Rotors for Size-Selective Capture of CO₂ from CH₄ and N₂,” *ACS Sustain. Chem. Eng.*, vol. 7, no. 3, pp. 3138–3144, 2019, doi: 10.1021/acssuschemeng.8b04916.
- [60] P. Freund *et al.*, “MIL-53(Al)/Carbon Films for CO₂ -Sensing at High Pressure,” *ACS Sustain. Chem. Eng.*, vol. 7, no. 4, pp. 4012–4018, 2019, doi: 10.1021/acssuschemeng.8b05368.
- [61] Z. Zhou *et al.*, “A novel bimetallic MIL-101(Cr, Mg) with high CO₂ adsorption capacity and CO₂/N₂ selectivity,” *Chem. Eng. Sci.*, vol. 7, no. 4, pp. 4012–4018, 2016, doi: 10.1016/j.ces.2016.03.035.
- [62] W. R. Lee *et al.*, “Exceptional CO₂ working capacity in a heterodiamine-grafted metal-organic framework,” *Chem. Sci.*, vol. 6, no. 7, pp. 3697–3705, 2015, doi: 10.1039/c5sc01191d.
- [63] Y. L. Wu *et al.*, “Synthesis of two new Cd(II)-MOFs based on different secondary building units with highly selective gas sorption for CO₂/CH₄ and luminescent sensor for Fe³⁺ and CrO₇²⁻ ions,” *Journal of Solid State Chemistry*, vol. 285. p. 121258, 2020, doi: 10.1016/j.jssc.2020.121258.
- [64] X. Chong, K. J. Kim, P. R. Ohodnicki, E. Li, C. H. Chang, and A. X. Wang, “Ultrashort Near-Infrared Fiber-Optic Sensors for Carbon Dioxide Detection,” *IEEE Sens. J.*, vol. 15, no. 9, pp. 5327–5332, 2015, doi: 10.1109/JSEN.2015.2438063.
- [65] M. S. Alivand, M. Shafiei-Alavijeh, N. H. M. H. Tehrani, E. Ghasemy, A.

- Rashidi, and S. Fakhraie, “Facile and high-yield synthesis of improved MIL-101(Cr) metal-organic framework with exceptional CO₂ and H₂S uptake; the impact of excess ligand-cluster,” *Microporous and Mesoporous Materials*, vol. 279, pp. 153–164, 2019, doi: 10.1016/j.micromeso.2018.12.033.
- [66] B. Chocarro-Ruiz *et al.*, “A CO₂ optical sensor based on self-assembled metal-organic framework nanoparticles,” *J. Mater. Chem. A*, vol. 6, no. 27, pp. 13171–13177, 2018, doi: 10.1039/c8ta02767f.
- [67] S. M. Majhi *et al.*, “Metal-organic frameworks for advanced transducer based gas sensors: Review and perspectives,” *Nanoscale Adv.*, vol. 4, no. 3, pp. 697–732, 2022, doi: 10.1039/d1na00798j.
- [68] F. Hillman, “Developing microwave-assisted synthesis for hybrid zeoliticimidazolate frameworks deriving from ZIF-8 for tunable gas separations,” 2019.
- [69] E. Hunter-Sellars, P. A. Saenz-Cavazos, A. R. Houghton, S. R. McIntyre, I. P. Parkin, and D. R. Williams, “Sol–Gel Synthesis of High-Density Zeolitic Imidazolate Framework Monoliths via Ligand Assisted Methods: Exceptional Porosity, Hydrophobicity, and Applications in Vapor Adsorption,” *Advanced Functional Materials*, vol. 31, p. 2008357, 2021, doi: 10.1002/adfm.202008357.
- [70] B. J. El Taher, R. Sabouni, and M. Ghommem, “Luminescent metal organic framework for selective detection of mercury in aqueous media: Microwave-based synthesis and evaluation,” *Colloids and Surfaces A: Physicochemical and Engineering Aspects*, vol. 607, p. 125477, 2020, doi: 10.1016/j.colsurfa.2020.125477.
- [71] INFICON, “Operating Manual Micro GC Fusion® Gas Analyzer,” 2017. [Online]. Available: [chrome-extension://efaidnbmnnnibpcajpcglclefindmkaj/https://www.inficon.com/media/5744/download/074-594-P1K_Micro_GC_Fusion_Operating_Manual_web_version.pdf?v=1&inline=true](https://www.inficon.com/media/5744/download/074-594-P1K_Micro_GC_Fusion_Operating_Manual_web_version.pdf?v=1&inline=true).
- [72] Y. Zhang, Y. Jia, and L. Hou, “Synthesis of zeolitic imidazolate framework-8 on polyester fiber for PM_{2.5} removal,” *RSC Advances*, vol. 8, pp. 31471–31477, 2018, doi: 10.1039/c8ra06414h.
- [73] S. Zhang *et al.*, “Carbonic Anhydrase Enzyme-MOFs Composite with a Superior Catalytic Performance to Promote CO₂ Absorption into Tertiary Amine Solution,” *Environ. Sci. Technol.*, vol. 52, pp. 12708–12716, 2018, doi: 10.1021/acs.est.8b04671.
- [74] W. S. Chi *et al.*, “Mixed matrix membranes consisting of SEBS block copolymers and size-controlled ZIF-8 nanoparticles for CO₂ capture,” *Journal of Membrane Science*, vol. 495, pp. 479–488, 2015, doi: 10.1016/j.memsci.2015.08.016.
- [75] C. J. Wijaya, S. Ismadji, H. W. Aparamarta, and S. Gunawan, “Facile and Green Synthesis of Starfruit-Like ZIF-L, and Its Optimization Study,” *Molecules*, vol. 26, p. 4416, 2021.
- [76] P. Khanh and N. T. Trung, “Understanding Interaction Capacity of CO₂ with

Organic Compounds at Molecular Level: A Theoretical Approach,” in *Carbon Dioxide Chemistry, Capture and Oil Recovery*, 2018.

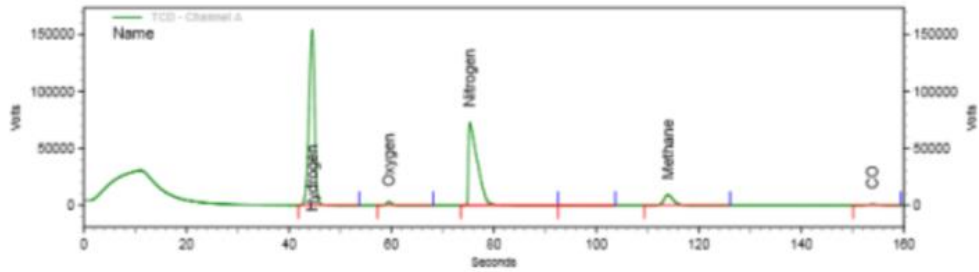
- [77] M. Polisi *et al.*, “CO₂ Adsorption/Desorption in FAU Zeolite Nanocrystals: In Situ Synchrotron X-ray Powder Diffraction and in Situ Fourier Transform Infrared Spectroscopic Study,” *J. Phys. Chem. C*, vol. 123, no. 4, pp. 2361–2369, 2019, doi: 10.1021/acs.jpcc.8b11811.
- [78] C. Nieto-draghi, G. Chaplais, and A. Simon-masseron, “Adsorption of CO₂, CH₄, and N₂ on Zeolitic Imidazolate Frameworks: Experiments and Simulations,” *Chem. Eur. J.*, vol. 16, pp. 1560–1571, 2010, doi: 10.1002/chem.200902144.
- [79] A. Mohamed, “CO₂ selective metal organic framework ZIF-8 modified through IL encapsulation: a computational study,” *Journal of computational science*, vol. 27, pp. 183-191, 2018.
- [80] H. P. S. Abdul Khalil *et al.*, “Barrier properties of biocomposites/hybrid films,” in *Mechanical and Physical Testing of Biocomposites, Fibre-Reinforced Composites and Hybrid Composites*, 2018, pp. 241–258.
- [81] A. Deacon *et al.*, “Understanding the ZIF-L to ZIF-8 transformation from fundamentals to fully costed kilogram-scale production,” *Commun. Chem.*, vol. 5, no. 18, 2022, doi: 10.1038/s42004-021-00613-z.
- [82] H. Misran, N. Mahadi, S. Z. Othman, Z. Lockman, and N. Amin, “Room Temperature Synthesis and Characterizations of ZIF-8 Formation at Water-Fatty Alcohols Interface Room Temperature Synthesis and Characterizations of ZIF-8 Formation at Water-Fatty Alcohols Interface,” *J. Phys. Conf. Ser.*, vol. 1082, no. 012046, pp. 8–14, 2018, doi: 10.1088/1742-6596/1082/1/012046.
- [83] B. The Huy, D. T. Thangadurai, M. Sharipov, N. Ngoc Nghia, N. Van Cuong, and Y. I. Lee, “Recent advances in turn off-on fluorescence sensing strategies for sensitive biochemical analysis - A mechanistic approach,” *Microchem. J.*, vol. 179, no. March, p. 107511, 2022, doi: 10.1016/j.microc.2022.107511.
- [84] S. Wang, B. Zang, Y. Chang, and C. Hongqi, “Synthesis and carbon dioxide capture properties of flower-shaped zeolitic imidazolate framework-L,” *CrystEngComm*, vol. 10, p. 1039, 2019.
- [85] N. Missaoui, H. Kahri, and U. B. Demirci, “Rapid room-temperature synthesis and characterizations of high-surface-area nanoparticles of zeolitic imidazolate framework-8 (ZIF-8) for CO₂ and CH₄ adsorption,” *J. Mater. Sci.*, vol. 57, no. 34, pp. 1–13, 2022.
- [86] Y. W. Abraha, C. W. Tsai, J. W. H. Niemantsverdriet, and E. H. G. Langner, “Optimized CO₂ Capture of the Zeolitic Imidazolate Framework ZIF-8 Modified by Solvent-Assisted Ligand Exchange,” *ACS Omega*, vol. 6, no. 34, pp. 21850–21860, 2021, doi: 10.1021/acsomega.1c01130.
- [87] C. Soodsuansi, S. Kulpratipunja, C. Ratanatawanate, and P. Rangsunvigit, “Adsorption of methane and carbon dioxide on activated carbon and ZIF-8 (Zeolitic Imidazolate Framework),” *Chemical Engineering Transactions*, vol. 70, pp. 1633–1638, 2018, doi: 10.3303/CET1870273.

- [88] Q. Liu *et al.*, “Metal-organic frameworks based fluorescent sensor array for discrimination of flavonoids,” *Talanta*, vol. 203, pp. 248–254, 2019, doi: 10.1016/j.talanta.2019.05.073.
- [89] S.-S. Lee, M. Sharipov, W. J. Kim, and Y.-I. Lee, “Turn Off–On Fluorescent CO₂ Gas Detection Based on Amine-Functionalized Imidazole-Based Poly(ionic liquid),” *ACS Omega*, vol. 7, no. 44, pp. 40485–40492, 2022, doi: 10.1021/acsomega.2c05695.
- [90] Meersens, “Indoor air quality: the impact of CO₂ on health and well-being at work.” <https://meersens.com/indoor-air-quality-the-impact-of-co2-on-health-and-wellbeing-at-work/?lang=en#:~:text=As%20can%20be%20seen%20in,cognitive%20abilities%20and%20reduces%20absenteeism.> [accessed Feb. 13, 2023].
- [91] W. Zhu, X. Li, Y. Sun, R. Guo, and S. Ding, “Introducing hydrophilic ultra-thin ZIF-L into mixed matrix membranes for CO₂/CH₄ separation,” *RSC Advances*, vol. 9, pp. 23390–23399, 2019, doi: 10.1039/c9ra04147h.
- [92] H. N. Abdelhamid, “Removal of carbon dioxide using zeolitic imidazolate frameworks: Adsorption and conversion via catalysis,” *Appl. Organomet. Chem.*, vol. 36, no. 8, p. e6753, 2022.
- [93] J. Guo *et al.*, “ZIF-8 induced growth of blade-like Zn nanosheets on carbon fiber cloth for high-performance separation of oil-in-water emulsion,” *J. Mater. Sci.*, vol. 57, pp. 15777–15788, 2022, doi: <https://doi.org/10.1007/s10853-022-07633-7>.
- [94] E. T. Sayed *et al.*, “A carbon-cloth anode electroplated with iron nanostructure for microbial fuel cell operated with real wastewater,” *Sustain.*, vol. 12, no. 16, p. 6538, 2020, doi: 10.3390/su12166538.
- [95] T. Unugul and F. U. Nigiz, “Preparation and Characterization an Active Carbon Adsorbent from Waste Mandarin Peel and Determination of Adsorption Behavior on Removal of Synthetic Dye Solutions,” *Water. Air. Soil Pollut.*, vol. 231, no. 538, 2020, doi: 10.1007/s11270-020-04903-5.
- [96] L. Ren *et al.*, “Efficient removal of formaldehyde with ZIF-8 growth on TiO₂-coated activated carbon fiber felts prepared via atomic layer deposition,” *J. Mater. Sci.*, vol. 55, no. 8, 2020, doi: 10.1007/s10853-019-04142-y.
- [97] R. Lin *et al.*, “Mechanochemically Synthesised Flexible Electrodes Based on Bimetallic Metal–Organic Framework Glasses for the Oxygen Evolution Reaction,” *Angew. Chemie - Int. Ed.*, vol. 134, no. 4, p. e202112880, 2022, doi: 10.1002/anie.202112880.

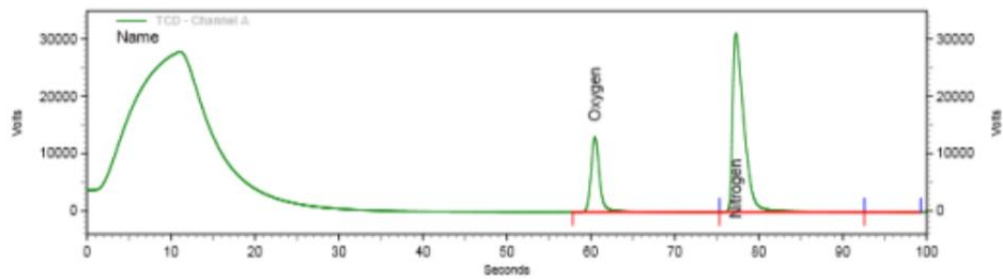
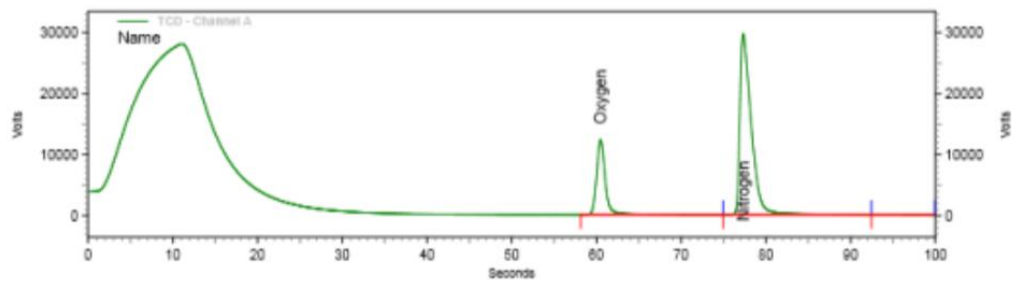
Appendix A

In this Appendix, the chromatogram figures obtained from GC analysis are shown:

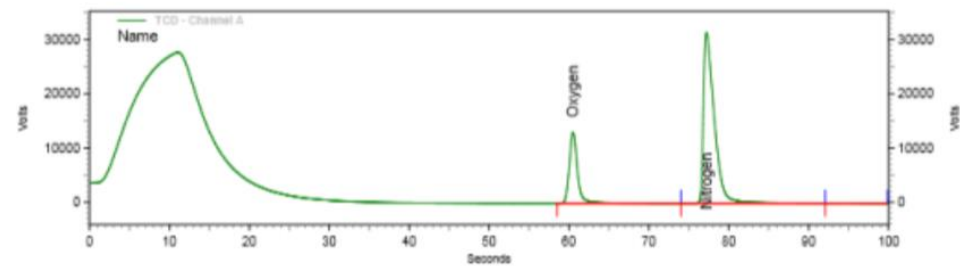
Calibration gas:

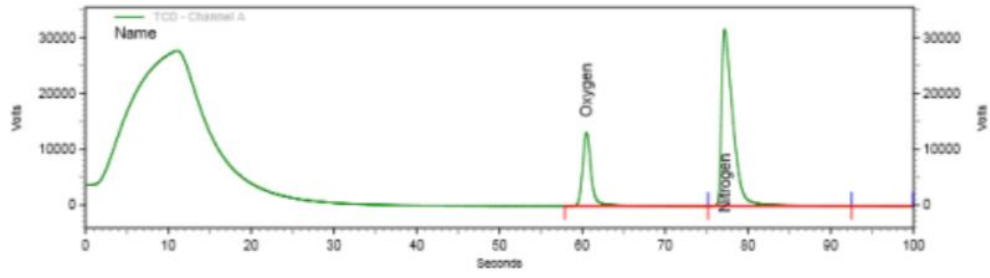


Carbon cloth sample:

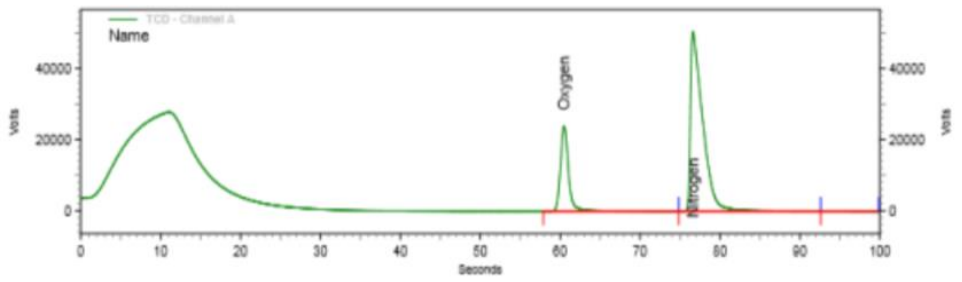
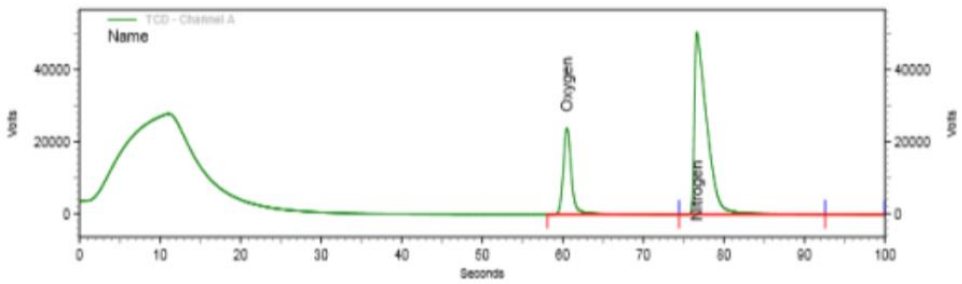


Coating1:

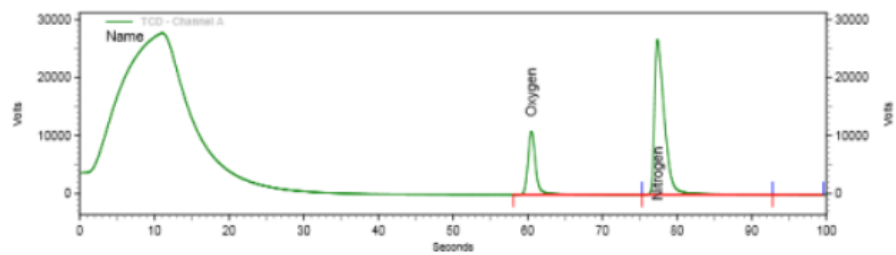
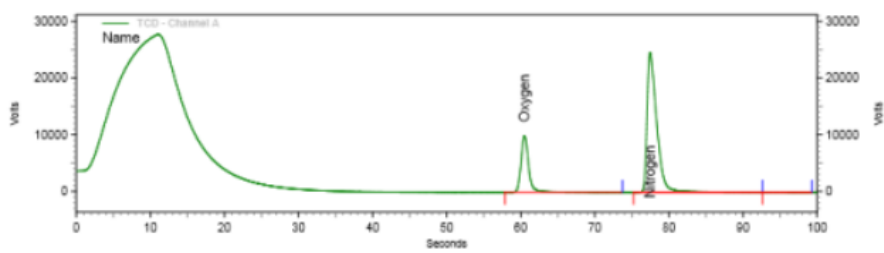




Coating 2:



Coating 3:



Vita

Shamma Al Abdulla was born in 1999, in Dubai, United Arab Emirates. She obtained her primary and secondary education in Dubai, UAE. She then obtained her B.Sc. degree in Sustainable and Renewable Energy Engineering from the University of Sharjah in 2021. She worked as a research assistant before joining the master's program.

In September 2021, she joined the Mechanical Engineering master's program in the American University of Sharjah as a graduate teaching and research assistant. During her master's study, she authored two papers related to her thesis which were presented in conferences. Her research interests are in CO₂ capture, CO₂ detection and synthesis of materials.